# The Role of Tides in Ocean-Ice Shelf Interactions in the Southwestern Weddell Sea

Ute Hausmann, Jean-Baptiste Sallée, Nicolas Jourdain, Pierre Mathiot, clement rousset, Gurvan Madec, Julie Deshayes, Tore Hattermann

# The role of tides in ocean–ice-shelf interactions in the southwestern Weddell Sea

**U. Hausmann[1,*], J.-B. Sallée[1], N. C. Jourdain[2], P. Mathiot[3], C. Rousset[1], G. Madec[1], J. Deshayes[1], and T. Hattermann[4,5]**

[1]Sorbonne-Université, LOCEAN-IPSL, Paris, France

[2]Univ. Grenoble Alpes/CNRS/IRD/G-INP, IGE, Grenoble, France

[3]Met Office, Exeter, United Kingdom

[4]AWI, Bremerhaven, Germany

[5]Norwegian Polar Institute, Framsentret, Postboks 6606, Langnes, 9296 Tromsø, Norway



**Key Points:**

- Near-observed Weddell Sea gyre, continental-shelf & cavity water masses in interactive ocean/sea-ice/tide/ice-shelf melt simulations
- Tides amplify basal melt-refreeze pattern, raising net melt by 50%, associated with enhanced time-varying kinetic energy at the ice base
- Impacts of additional meltwater production on Weddell continental shelf sea ice and newly formed bottom water properties are suggested

*Corresponding author: U. Hausmann, uhausc at gmail dot com

This article has been accepted for publication and undergone full peer review but has not been through the copyediting, typesetting, pagination and proofreading process which may lead to differences between this version and the Version of Record. Please cite this article as doi: 10.1029/2019JC015847

**Abstract**

To investigate the role of tides in Weddell Sea ocean–ice-shelf-melt interactions, and resulting consequences for ocean properties and sea-ice interactions, we develop a regional ocean–sea-ice model configuration, with time-varying ocean boundary and atmospheric forcing, including the deep open ocean (at 2.5-4 km horizontal resolution), the southwestern continental shelf ($\approx$ 2.5 km), and the adjacent cavities of eastern Weddell, Larsen and Filchner-Ronne ice shelves (FRIS, 1.5-2.5 km). Simulated circulation, water mass and ice-shelf melt properties compare overall well with available open-ocean and cavity observational knowledge. Tides are shown to enhance the kinetic energy of the time-varying flow in contact with the ice shelves, thereby increasing melt. This dynamically-driven impact of tides on net melting is to almost 90 % compensated by cooling through the meltwater that is produced but not quickly exported from regions of melting in the Weddell Sea cold-cavity regime. The resulting systematic tide-driven enhancement of both produced meltwater and its refreezing on ascending branches of, especially the FRIS, cavity circulation acts to increase net ice-shelf melting (by 50 % in respect to the state without tides, $\approx$ 50 Gt/yr). In addition, tides also increase the melt-induced FRIS cavity circulation, and the meltwater export by the FRIS outflow. Simulations suggest attendant changes on the open-ocean southwestern continental shelf, characterized by overall freshening and small year-round sea-ice thickening, as well as in the deep southwestern Weddell Sea in the form of a marked freshening of newly-formed bottom waters.

# 1 Introduction

The polar sector of the Southern Ocean and its interaction with the cryosphere plays a key role in the global climate system. Ocean–ice-shelf interactions and the associated ice-shelf basal melt are an important cause of the Antarctic ice-sheet mass loss, which is currently accelerating, and is of global concern for current and future sea-level rise (e.g. *The IMBIE team*, 2018). Ocean–sea-ice–ice-shelf interactions form the densest water masses of the world ocean that sink, fill the bottom of the world ocean, and represent an important engine for the global ocean

overturning circulation. In spite of their importance for climate, these intricate interactions and associated mechanisms are still poorly understood, and represent one glaring uncertainty in our current knowledge of climate and its changes.

An important block to our understanding of the impact of these polar processes at global scale is the scarcity of polar Southern Ocean observations due to its remoteness, the seasonal presence of sea ice, harsh meteorological conditions, and the difficulties of sampling its ice-shelf cavities. In addition, the current generation of global climate models does not include ocean–ice-shelf interactions, which further limits our process understanding. Recent studies that do account for some of these processes predict, however, considerable global climate impacts and important associated climate feedbacks (*Bronselaer et al.*, 2018; *Golledge et al.*, 2019). Adequate regional modelling tools that capture this regional ocean and its interaction with sea ice and ice shelves are thus called for, to improve our understanding of the physical processes at play, to enable understanding of variability and predictions of responses to change, as well as to inform the accurate representation of these processes in the next generations of global climate models.

Here, we present a new regional ocean–sea-ice model configuration of the Weddell Sector of the Southern Ocean, including open-ocean gyre, continental shelf, and cavity ocean interactions with melting ice shelves in presence of tides. The Weddell Sea hosts the largest ice-shelf by volume (the Filchner-Ronne Ice Shelf; FRIS), as well as the largest production of Antarctic Bottom Water (*Orsi et al.*, 1999), parts of which are exported through its deep northern passages (e.g. *Heywood*, 2004) shaping global ocean bottom properties (e.g. *Orsi et al.*, 2002; *Jullion et al.*, 2014; *Purkey et al.*, 2018). Whereas currently Weddell Sea ice shelves, to the exception of the Larsen ice shelves adjacing the peninsula, are observed to be amongst the most stable (*Rignot et al.*, 2019; *Schröder et al.*, 2019), the region features some of the largest uncertainties in long-term predictions of ice-shelf melting and thereby sea-level contribution (e.g. *Nowicki and Seroussi*, 2018; *The IMBIE team*, 2018; *Shepherd et al.*, 2018). Recent modelling results indeed predict the possibility of drastic (and possibly irreversible) changes in local ocean–ice-shelf interactions (*Hellmer et al.*, 2012, 2017; *Naughten et al.*, 2018a), with, if to occur, consequences for global ocean water-mass properties (*Golledge et al.*, 2019) and the (East) Antarctic ice sheet

(*Timmermann and Goeller*, 2017).

One of the outstanding characteristics of the southwestern Weddell Sea is that it, and especially its continental shelves and ice-shelf seas, features some of the Southern Ocean's most intense tides. The maximum tidal ranges is in excess of 2 m nearly everywhere in the region, peaking at more than 6 m in the FRIS cavity and featuring several zones of intense tidal currents reaching 1 m/s (e.g. *Padman et al.*, 2018), as known from point-wise observations (e.g. *Foldvik et al.*, 1990; *King et al.*, 2011) and barotropic tide-only modelling (*Robertson et al.*, 1998; *Makinson and Nicholls*, 1999). The presence of these intense tidal circulations is now known to play an important role in ice-shelf dynamics and their exchanges with the ocean (e.g. review by *Padman et al.*, 2018). In particular, previous modelling work has identified that tides play a key role in the region in terms of exchanges between the ice-shelf cavity and the open ocean, as well as the mixing of water masses on the continental shelf (*Makinson and Nicholls*, 1999), and the exchange of water-masses across the continental slope (*Robertson*, 2001a; *Pereira et al.*, 2002; *Stewart et al.*, 2018). Nonetheless, simulations of tides in interaction with the Weddell open and cavity ocean circulation are so far limited to idealized configurations without basal melting (*Robertson*, 2001a,b), a small single ice-shelf subdomain (*Mueller et al.*, 2012), or idealized forcing. In particular, the two regional ocean-tide modelling studies of the large FRIS cavity and its adjacent shelf, used either a homogeneous cold or warm shelf state (*Mueller et al.*, 2018), or thermohaline restoring on the continental shelf with a fixed spatial pattern and an idealized seasonal modulation (*Makinson et al.*, 2011), and did not include substantial deep open-ocean regions. Here, we go one step further by introducing a new realistic configuration of the Southern Weddell Sea sector to address the impact of tides on ice-shelf melting, unveil the processes at play, and investigate the consequences in terms of ocean water-mass characteristics resulting from the ocean-cryosphere interaction in the presence of tides.

A large part of our current knowledge of ocean–sea-ice–ice-shelf interactions stems today from regional numerical configurations not including tides (*Dinniman et al.*, 2016; *Asay-Davis et al.*, 2017). In the Weddell Sea, in particular, several ocean circulation model configurations have been developed including FRIS (*Jenkins and Holland*, 2002; *Jenkins*, 2004; *Gerdes et al.*, 1999;

*Beckmann et al.*, 1999; *Timmermann et al.*, 2002). These simulations were usually done at relatively coarse resolution and often hid the effects of the non-resolved tidal (and non-tidal) circulation on ice-shelf melting in an empirical constant heat exchange velocity (e.g. *Timmermann et al.*, 2002). More recently, global configurations focussing resolution around the Weddell Sea or circumpolar configurations resolving Antarctic ice-shelf cavities have also been developed (*Dinniman et al.*, 2015; *Timmermann et al.*, 2012; *Timmermann and Hellmer*, 2013; *Losch*, 2008; *Schodlok et al.*, 2016; *Mathiot et al.*, 2017). The increasing number of numerical models and configurations starts to allow for intercomparison studies (*Naughten et al.*, 2018b), which begin to shed first light on model dependency, and are, overall, instrumental in refining our understanding of the polar Southern Ocean and its role for climate. Our study complements that diversity of realistic model configurations, and introduces how tides influence the complex ocean–sea-ice–ice-shelf coupled system. The southwestern Weddell Sea configuration designed here features relatively high horizontal resolution ranging from 4.5 km to 1.5 km, with interannually-varying ocean boundary and atmospheric surface forcing, acting on an ocean model coupled to a dynamic-thermodynamic sea-ice model. It captures not only FRIS but also other Weddell cavity systems, namely the Larsen ice shelves downstream and the eastern Weddell ice shelves (EWIS) upstream, and their interaction with the adjacent open continental shelves, and, through the slope front system, the deep open-ocean Weddell gyre (Fig. 1).

The model configuration and the experiments designed and analyzed in this study are described in detail in section 2. Simulated ocean – sea-ice – ice-shelf melt interactions in the tidal reference experiment are presented in section 3, including comparisons to available observational estimates. The role of tides in shaping ocean – ice-shelf melt interactions is explictely assessed, by making use of a non-tidal sensitivity experiment, in section 4, which allows to investigate the physical mechanisms of the tidal impact and assesses wider-reaching impacts of the tide-induced changes on the Weddell climate system. Section 5 provides discussion of results, in particular in comparison to previous modelling, before section 6 concludes.

# 2 Southwestern Weddell model configuration, experimental design and observational datasets

This section presents the new model configuration (section 2.1) and the experiments (section 2.2) designed for the present study, and introduces various observational datasets discussed in the following in comparison to model results (section 2.3).

## 2.1 Southwestern Weddell Sea model configuration

The coupled ocean–sea-ice model configuration of the southwestern Weddell Sea developed here includes ice-shelf cavities, continental shelves & the deep open ocean, at a horizontal resolution varying from 4.5 km at 60°S to 1.5 km at the southernmost location in the Ronne cavity (Fig. 1). It is forced at the surface with an interannually varying atmosphere, at the boundaries with interannually varying ocean and sea-ice states as well as tides, all interacting with ice-shelf basal melting in resolved ice-shelf cavities (a detailed presentation of the experimental design choices of the present study follows in section 2.2).

The coupled ocean–sea-ice model used is NEMO (Nucleus for European Modelling of the Ocean) 3.6 (*Madec and NEMO-team*, 2016), with the sea-ice model LIM (Louvain-la-Neuve sea-ice model) 3.6, a dynamic-thermodynamic multi-category multi-layer sea-ice model with elastic-viscous-plastic rheology (*Vancoppenolle et al.*, 2009; *Rousset et al.*, 2015), which is used here with 5 ice categories with 5 ice layers each. NEMO's ocean component is a primitive equation, Boussinesq model on an Arakawa-C grid with a nonlinear equation of state (here we use polynomial TEOS-10; *IOC et al.*, 2010; *Roquet et al.*, 2015) and a free surface, which we use here in its nonlinear form, and with a split-explicit formulation of the surface pressure gradient. Corresponding water column thickness variations are distributed through depth with a time-dependant z*-coordinate (*Adcroft and Campin*, 2004), which has been adapted for the presence of ice shelves, impacting horizontal ocean pressure gradients and modelled here as floating in hydrostatic equilibrium, by *Mathiot et al.* (2017).

Ice shelves in NEMO, as implemented by *Mathiot et al.* (2017), and so far employed in a global and an Amundsen regional configuration by *Storkey et al.* (2018) and *Jourdain et al.* (2017), are dynamically passive, that is ice loss/gain due to basal melt/freeze are assumed to be instantaneously equilibrated by ice convergence. This assumption of a static ice-shelf geometry is a good approximation for simulations on time scales of a few years and decades. The ocean interacts with ice-shelf basal melting, by driving, and in turn responding to the induced, ice-shelf melt freshwater and heat fluxes, thermodynamically, and also dynamically through the meltwater-induced oceanic volume divergence. The thermodynamic interaction, made possible by the introduction of a diagnostic ice-shelf base interface layer into ocean models as pioneered by *Hellmer and Olbers* (1989), is parameterized through a three-equation bulk formulation (*Holland and Jenkins*, 1999; *Jenkins et al.*, 2010; *Mathiot et al.*, 2017). In this, the oceanic turbulent heat flux $Q_{tbl}$ flowing upward out of the oceanic cavity top boundary layer (tbl) towards the ice-shelf base ($b$) depends not only on the ocean thermal driving (given by difference of temperature $T$ between tbl and ice base, b), but also on the oceanic tbl current speed $c_{tbl}$, as follows

$$Q_{tbl} = \rho_w c_{pw} St_T c_{tbl} \left(T_{tbl} - T_b\right), \tag{1}$$

and $\rho_w$ and $c_{pw}$ are ocean reference density and heat capacity, and $St_T$ the thermal Stanton number. Compared to earlier parameterizations (e.g. *Hellmer and Olbers*, 1989), this velocity dependence of turbulent exchanges has been found to more closely match observations and be more physically consistent (*Dansereau et al.*, 2014). As in the reference experiment of *Jourdain et al.* (2017), here we use a constant thermal Stanton number $St_T = 0.7 \times 10^{-3}$ in Eq. (1) and also keep the ratio of thermal and saline Stanton numbers fixed at 35 in the tbl equations. Simulated melt rates, and related circulation patterns, are sensitive to $St_T$, a sensitivity that has been assessed by *Jourdain et al.* (2017) and is not further explored in this study. The parameterization is applied here to a tbl of 30m thickness (or of the thickness of the top ocean cell where thicker), and other parameter choices, including the freezing-point linearization adapted to TEOS-10 ($\lambda_{1,2,3}$), are also as in *Jourdain et al.* (2017, cf. their Table 1). Although a simplistic representation that cannot fully account for the dynamic nature of the tbl (*Asay-Davis*

*et al.*, 2017; *Jenkins*, 2016), this bulk parameterization remains to date the typical formulation of melt interactions in ocean models with resolved cavities (cf. *Dinniman et al.*, 2016; *Asay-Davis et al.*, 2017, for reviews). Furthermore, as common in ocean–ice-shelf melt interactive modelling, the formation of frazil ice is not explicitely represented (e.g. *Bombosch and Jenkins*, 1995), nor is the impact of anticipated spatial heterogeneity in icedraft roughness, and especially its contrasts between melt and freeze regions, on basal melting accounted for (e.g. *Gwyther et al.*, 2015).

Ocean model physical parameterizations are also mostly as in *Jourdain et al.* (2017; Suppl. Table S1 lists the few key differences, and provides links to detailed information on the complete sets of choices). Thereby, momentum is advected using an energy- and enstrophy-conserving vector-form scheme, subject to along-geopotential bilaplacian viscosity, and removed through nonlinear bottom and top (under-icedraft) friction, with a frictional drag that varies logarithmically with last model layer depth (e.g. *Dansereau et al.*, 2014, cf. Table S1). Tracers are advected via a flux-corrected transport scheme, and subject to Laplacian iso-neutral diffusion. The vertical eddy diffusivity is $2.0 \times 10^{-6}$ m$^2$/s (modulated by a horizontal shape function), and effective vertical mixing is obtained via a turbulent kinetic energy closure scheme. Enhanced vertical tracer diffusion is furthermore applied in cases of static instability (cf. Table S1).

Our regional configuration uses an isotropic $1/12^\circ$ modified Mercator grid (referred to as eORCA12 in the NEMO community, *Mathiot et al.*, 2017) resulting in a horizontal resolution varying from about 4.5 km at the northern boundary of the gyre, 4 to 2 km over the continental shelves, to less than 2 km in the FRIS cavity (Fig. 1). Thereby it is at the limit of resolving the first baroclinic Rossby radius $R_d$ (of the reference simulation, not shown) in the deep gyre interior as well as the deep Filchner Trough ($R_d$ 4-8 km). On the continental slope and deeper parts of the continental shelves resolution is close to $R_d$ (4-2 km), whereas over shallower areas and in large part of the cavities $R_d$ can be an order of magnitude smaller than the grid scale ($\leq 1$ km). While thus not all mesoscale eddies and their effects on cross-shelf (e.g. *Stewart and Thompson*, 2015) and potentially cross-icefront (*Årthun et al.*, 2013) transports are resolved in the current configuration, it is substantially more eddying than other previous ocean–ice-shelf

model configurations including the Weddell region. Whereas eddy contributions to cross-icefront exchanges have to date not been assessed in realistic modelling studies, a short eddy-resolving simulation (*Stewart et al.*, 2018) suggests that for ocean-shelf heat transport in the Weddell Sea the role played by eddying circulations (with timescales >1-day) may be smaller than the roles of the mean circulation and tides. Here neither the Gent-McWilliams parameterization nor parameterizations for smaller-scale surface mixed-layer eddy effects (*Fox-Kemper et al.*, 2011) are used, as eddies are partly resolved over large parts of the domain (and also since interplay with ice shelves requires further developments, in which partial domain parameterizations following e.g. *Hallberg*, 2013, may be useful).

Vertically 75 levels yield a resolution varying from 1 m at the surface, 10–150 m beneath ice shelves and 200 m at 6 km depth (*Mathiot et al.*, 2017). The bathymetry is derived from a combination of ETOPO1 in the open Southern Ocean, IBCSO over the Antarctic continental shelves and BEDMAP2 in ice-shelf cavities for bathymetry and icedraft (as described in *Mathiot et al.*, 2017, and references therein), before interpolation to the model grid. Bottom and top partial cells are used to better approach bathymetry and icedraft, and the effective model bathymetry and icedraft (Fig. 1) are modified to eliminate vertically unresolved cavity zones. Here the inclusion of tides has been found to furthermore require a minimum initial water column thickness of 10 m (across two partial-cell layers) to achieve numeric stability and accommodate the tide-induced oscillations of water depth under the hydrostatically floating ice shelves.

The domain chosen here (pink lines in Fig. 1) covers roughly the southwest quarter of the asymmetric Weddell gyre (e.g. *Gouretski and Danilov*, 1993; *Orsi et al.*, 1993), with an eastern boundary placed just west of 0°E and a main northern boundary that passes near the northwestern deep escape passages through the South Orkney Islands, i.e. near or to the south of the southern boundary of the ACC (e.g. *Orsi et al.*, 1995; *Heywood*, 2004). In the northwestern corner of the domain, a small western segment of the northern open boundary links the tip of the Antarctic peninsula to Joinville Island, and a western boundary traverses Bransfield Strait from Joinville Island to the South Shetland Islands, from where the major segment of the northern boundary extends eastward. Along the open lateral boundaries the model bathymetry is modified to match

that of the lateral forcing simulation over a transition zone (as in *Jourdain et al.*, 2017), and the ice-shelf cavity passages linking towards Fimbul along the eastern boundary are grounded (east of the solid pink line in Fig. 1), making Jelbart (without its cavity passages towards Fimbul) the easternmost resolved cavity of the current configuration. Following the gyre, the model domain includes three major ice-shelf formations: (1) the eastern Weddell ice shelves EWIS, with a total model surface of $94\times10^3$ km$^2$ and a maximum model ice draft of almost 900 m, include Jelbart, Atka, Ekstroem, Quar and Riiser-Larsen ice shelves and the Brunt/Stancomb-Wills ice-shelf system; (2) FRIS with Filchner and Ronne ice shelves covers $425\times10^3$ model km$^2$ reaching to a peak depth of $\approx$ 1700 m; and (3) the Larsen ice shelves along the peninsula, with a model surface of $63\times10^3$ km$^2$ and a shallower maximum depth of $\approx$ 500 m, are Larsen G, F, E, D, C, as well as the remnant of B after its 2002 breakup, the SCAR inlet glacier, and the remnant of A after its 1995 breakup, the Seal Nunatak Glacier (Fig. 1).

## 2.2 Experimental design

In the experiment used as reference here the Weddell Sea regional configuration introduced above is constrained at its lateral open boundaries with tides (as detailed below) as well as interannually-evolving ocean and sea-ice states from a global $1/4^\circ$ coupled ocean–sea-ice simulation with resolved ice-shelf cavities (GO7, *Storkey et al.*, 2018, not including tides and with basal melt rates prescribed using the satellite-derived estimate by *Rignot et al., 2013*). The GO7 lateral ocean boundary conditions are imposed as monthly means, using a flow relaxation scheme for temperature, salinity and baroclinic velocities, and the Flather radiation scheme for sea-surface height and barotropic velocities, applied without regional volume control to allow for tides (see *Madec and NEMO-team*, 2016).

Here simulations are initialized with a monthly-average temperature & salinity state from GO7 (January 1990 namely). This implies a physically consistent regional ocean initial state throughout the domain including its cavities, obtained via a 14-year spinup in the global $1/4^\circ$ GO7 experiment prior to the start of our regional simulations (the GO7 simulation is initialized in

1976 from a 1995-2014 climatology of the EN4 objective analysis, *Good et al.*, 2013, extrapolated into the opened ice-shelf cavities).

For consistency, atmospheric surface-boundary conditions are taken as in the boundary-forcing simulation, from CORE-2 (*Large and Yeager*, 2009) applied via CORE bulk formulae. Additionally, the surface-freshwater forcing of drifting and melting icebergs is prescribed using interannually-varying monthly-average outputs of GO7's Lagrangian iceberg model (*Marsh et al.*, 2015), itself fed along the Antarctic coasts by an iceberg calving-flux climatology (*Rignot et al.*, 2013). Furthermore, solar radiation is parameterized to penetrate through depth (*Madec and NEMO-team*, 2016) depending on prescribed seasonally-varying climatological chlorophyll-A concentrations (derived from SeaWIFS, *O'Reilly et al.*, 1998). Note that, whereas remote effects of sea-surface salinity restoring, which is applied globally in GO7, are imported through the lateral boundaries, within the regional domain no surface restoring is used in this study.

Regarding sea ice, GO7 monthly-average interannually-varying sea-ice concentration, thickness and snow thickness are imposed along the open boundaries (via flow relaxation). Sea ice is also initialized, using above properties capped at 99.7 % ice concentration and thicknesses of 4 m for ice and 50 cm for snow (both for numerical stability and consistency with available observational constraints – GO7 has rather thick sea ice near the ice-shelf edges, especially where ice-shelf waters outflow), as well as in addition ice-surface temperature and ice-depth-average salinity (initial ice-depth-average temperature is set to the average of ice-surface temperature and $-1.9^{\circ}$C).

Tidal elevations and currents along the open-ocean boundaries are imposed using phases and amplitudes of 18 tidal constituents from FES2012 (*Carrère et al.*, 2012; *Lyard et al.*, 2006), a global finite-element solution of the tidal barotropic equations resolving ice-shelf cavities and assimilating multi-satellite altimetry (note this does not involve many data in the ice-covered Southern Ocean). In comparison to the still sparse tidal records available over Antarctic continental margins and ice shelves, tide models, including FES2012, still show rms errors of typically 15-30 % for the major tidal constituents (*Stammer et al.*, 2014). Indeed, comparing tidal

elevation timeseries from GPS-based tide gauge records for two sites on FRIS with reconstruction using five contemporary tide models, including FES2012, reveals instantaneous local model errors up to 40 cm (*King et al.*, 2011, see *Stammer et al.* (2014) *their Figure 7*). Whereas this is not satisfactory for tidal prediction, such errors are superimposed on tidal elevations of up to 2 m underneath FRIS, and the zero-order tidal signal is overall well represented in both timing and amplitude by all the models including FES2012. Here, furthermore, FES2012 outputs are not used directly underneath ice shelves, but only along the open boundaries of the regional domain, where smaller errors are anticipated, as closer to the regions of data assimilation in FES2012. From the boundaries, the ocean model propagates the tidal signals throughout the domain in full interaction with the three-dimensional oceanic circulation. *Jourdain et al.* (2019), for their Amundsen Sea regional configuration, have shown that the resulting simulated tidal signals compare well with those of the input tidal model near the continental shelf break and underneath ice shelves. Nonetheless it is likely that some localized features of the tidal circulation especially in cavities will be missing or misrepresented, if only due to imperfections in bathymetry and icedraft datasets and their discretizations (e.g. *Padman et al.*, 2018; *Rosier et al.*, 2018). As in the most complex simulation of *Jourdain et al.* (2019), here we use 18 tidal constituents. These include the 8 major constituents in the Weddell region, namely the four primary, M2, S2, K1, O1, followed by K2, N2, P1, Q1 (*King et al.*, 2011), as well as in addition S1, 2N2, $\mu 2$, $\nu 2$, L2, T2, M4, Mtm, Mf and Mm (e.g. *Schureman*, 1958).

In summary, the regional-configuration reference experiment designed here differs from the global simulation, which is imposed at its open-ocean boundaries and provides a 14-year lower-resolution spinup prior to initializing the former, in three key ways: (i) allowing interactions of the ocean with ice-shelf basal melting, (ii) a higher horizontal resolution, thus capturing smaller-scale oceanic-circulation features, and (iii) the explicit inclusion of tides.

With this reference experiment design, a simulation of 8 years, 1990–1997, is run with an ocean-model time step of 4 minutes and a sea-ice-model and surface-forcing time step of 12 minutes. As discussed below (section 3, Fig. 2), simulated integral ice-shelf melt displays a spinup of $O$(1 year), and the analysis will mostly focus on the last 5 years of the 8-year

simulation (1993–1997). In addition, one perturbation experiment is realized here to investigate the role of tides in setting circulation, water-mass structure and Weddell Sea ocean–ice-shelf interactions, by repeating exactly the 8-year reference simulation, but without imposing any tidal boundary forcing. We note that all other experiment and parameterization choices, including the dissipation applied, are unchanged between the two experiments.

## 2.3 Observation-based datasets

To assess model integral ice-shelf melt rates we compare to observation-based estimates provided for individual ice shelves or groups of ice shelves by *Rignot et al.* (2013), *Depoorter et al.* (2013) and *Moholdt et al.* (2014). These estimates, representative of the late 2000s, are obtained using surface mass balance modelling and satellite-based estimates of grounding-line and icefront-calving fluxes, from which basal mass budgets are inferred, either assuming steady state for the Weddell ice shelves (*Depoorter et al.*, 2013), or furthermore invoking altimetry-derived ice-shelf thickness changes obtained using Eulerian (*Rignot et al.*, 2013) or Lagrangian (*Moholdt et al.*, 2014) methods.

For sea ice, are concentration maps combining measurements from various satellite microwave radiometers and imagers (SMMR, SSM/I & SSMIS, converted using the bootstrap algorithm version 2) are obtained as monthly means from nsidc.org/data/nsidc-0079/versions/2 (*Comiso*, 2000, updated 2015) for the simulation period. Weddell sea-ice area coverage timeseries are obtained by integrating sea-ice area concentration data on their native 25 x 25 km polar-stereographic grid across the regional model domain using a concentration threshold of 15 %.

To analyze open-ocean water-mass properties in comparison to the observed open-ocean hydrography, we use available individual in-situ temperature & salinity data from conductivity-temperature-depth (CTD) profiles acquired post 1972 within the model regional domain, compiled as a collection of profiles obtained from the NOAA World Ocean Database (www.nodc.noaa.gov/OC5/SELECT/dbsearch/dbsearch.html), the Pangea database

(www.pangaea.de), the Coriolis Argo international program GDAC (ftp://ftp.ifremer.fr/ifremer/argo), and the MEOP instrumented seal consortium (www.meop.net/). We only use profiles that have a quality control flag of 1, containing information on their position, date, temperature, and salinity profiles. Profiles are converted to conservative temperature and absolute salinity using the TEOS-10 tools (*IOC et al.*, 2010). Regarding FRIS cavity water masses, under ice-shelf CTD profile data from hot-water drill sites (mapped in Fig. 1) have been obtained as profiles through depth, covering most of the water column, at different times, during December 1990 at Site 1 (S1, *Nicholls et al.*, 1991), January 1992 at Site 2 (S2, *Robinson et al.*, 1994), January 1996 at Site 3 (S3, *Nicholls et al.*, 1997), December 1998 at Sites 4 and 5 (S4 and S5, *Nicholls et al.*, 2001), as well as in December 2002 at F2 and F3 and January 2003 at F1 and F4 (*Nicholls et al.*, 2004), and in January 2016 at FSW1, FSW2, FSE1, FSE2, and in December 2016 at FNE1, FNE2 and FNE3 (*Huhn et al.*, 2018).

# 3 Characterizing circulation and water masses in the reference experiment

The circulation and water masses of the reference experiment, i.e. including tides (cf. section 2), are now assessed, and discussed in comparison to key observation-derived metrics. Investigation of the role played by this tidal forcing, and discussion in comparison to previous modelling studies, follows below (sections 4 and 5).

**Ice-shelf melting** Reference experiment integral timeseries of ice-shelf melting are displayed in Fig. 2a (in gigatons per year, Gt/yr, with melting $<0$) for the three ice-shelf formations within the Weddell regional domain (cf. Figs. 1 & 3): EWIS (cyan), FRIS (red) and Larsen (green). At initialization, regional interactive model melt rates increase drastically from the prescribed melt of the global parent simulation (GO7, cf. section 2.2, indicated by triangles at the time-axis origin in Fig. 2a), by about 150 Gt/yr for each EWIS and Larsen, and by more than 250 Gt/yr for FRIS, within the first 5 days of the simulation (note 45-day running means are displayed in Fig. 2a).

This is followed by a slower adjustment phase in which regional integral melt rates decrease back from their initial peak and which lasts about one year (Fig. 2a).

For each ice-shelf formation, substantial variability in model basal melt is observed on a range of timescales, including clear variability from year to year, between seasons, and on higher eddying and tidal frequencies. A sample of the latter are indicated in Fig. 2a by standard-deviation envelopes around the 45-day running means (note that overall similar results are obtained varying the running mean length between 30 and 60 days). These standard deviations include variability at all frequencies between 5 and 45 days, which contains the imprint of tidal-driven variability due to aliasing of tides. While we note that the full tidal-driven melt variability is expected to be larger than indicated by the standard deviations in Fig. 2a, we do not aim here at documenting its exact amplitude, which would require much higher frequency outputs and is beyond the scope of the main objective here.

For the chosen set of parameters in Eq. (1), model integral ice-shelf melt rates are close to available recent observational estimates (displayed with their respective errorbars on the rhs of Fig. 2a). In particular time-average net model melt rates (shown in Table 1, using the last 5-year average of the 8-year reference simulation, i.e. 1993–1997) fall within the bracket of the *Rignot et al.* (2013) observational estimate (obtained for the late 2000s, see circles on rhs of Fig. 2a) for each of the three Weddell ice-shelf formations considered, if slightly on the high end for EWIS. For FRIS, model average net melt rates (159$\pm$28 Gt/yr, where the minus sign, indicating net melting, i.e. a negative basal mass balance, in Figures and Tables, is omitted here and as follows in the text) are close to both the *Rignot et al.* (2013, 155$\pm$43 Gt/yr) and the *Moholdt et al.* (2014, 124$\pm$66 Gt/yr) estimates, and higher than the steady-state estimate by *Depoorter et al.* (2013) of 50$\pm$40 Gt/yr, the latter being much lower than the other recent non-steady state estimates. Integral FRIS model average melt rates are also consistent with a recent estimate based on noble gases and thereby independent of those by glaciological studies (at 177$\pm$95 Gt/yr; *Huhn et al.*, 2018).

Fig. 2b compares timeseries of ice-shelf melt freshwater fluxes for the Weddell domain total

(pink) to the freshwater released by icebergs melting throughout the domain (black). Note the latter is imposed here as freshwater flux obtained from the Lagrangian iceberg model of the boundary forcing simulation and thus in the absence of tides and at lower ocean resolution (see section 2.2). In comparison to ice-shelf melt, iceberg melt shows larger seasonal and interannual variability, whereas ice-shelf melt shows larger high-frequency variability (standard deviation envelopes) due to the presence of tides. In the time average (Table 1), modelled Weddell total net basal melting (257$\pm$63 Gt/yr) is slightly smaller than domain-integral iceberg melting (275$\pm$220 Gt/yr).

The integral melt rates discussed so far arise from a spatially heterogenous pattern featuring regions of large and opposing basal melting and freezing (Fig. 3a). For the shallower ice shelves of EWIS and Larsen, refreezing is generally small. Here enhanced melting at average melt rates of typically 2-4 m/yr water equivalent (m.w.e/yr in the following) occurs near the ice fronts. For FRIS enhanced basal melting with peaks above 7 m.w.e/yr occurs near the grounding lines of several icestreams, as well as to the south of Berkner Island (81°S/55°W) and near the eastern Ronne icefront (77.5°S/50°W). Refreezing is pronounced and occurs to the north of Korff and Henry ice rises and rumples under central Ronne (79°S/62°W), as well as in association to the outflows on the western sides of both Filchner and Ronne Troughs (78.5°S/43°W and 75.5°S/63°W respectively). This pattern of simulated FRIS basal melting and freezing agrees very well, in both sign and magnitudes, with observational estimates by *Rignot et al.* (2013) & *Moholdt et al.* (2014), mapped for comparison in Fig. 3c&d. Whereas in these estimates refreezing on the western margin of Ronne is only estimated to occur deeper in the cavity, rather than reaching all the way to the icefront as simulated here, this is also where observational errorbars are amongst the largest (e.g. *Moholdt et al.*, 2014, their Fig. 10). Timeseries of basal melting and freezing, integrated separately over the regions where and when they occur, roughly mirror each other in their variability (not shown), suggesting a tight physical link of refreezing responding to melting without much timelag as part of the cavity mass overturning circulation / ice pump. Whereas integral refreezing is small under the small shallow ice shelves (typically $\leq$ 6% of the melting), it amounts to more than a third of the melt underneath FRIS in the

time-average (Table 1). The modelled FRIS glacial-ice/meltwater mass overturning rate (with freezing of 89±10 Gt/yr and melting of 248±35 Gt/yr, and thus a freeze/melt ratio of 36 %) is thereby very close to its observational estimate by *Moholdt et al.* (2014, of 77±25 Gt/yr basal accumulation vs 201±41 Gt/yr ablation, and thus a ratio of 38 %). Comparison to previous modelling estimates is provided in the discussion.

**Sea ice** Weddell domain integral sea-ice concentration (Fig. 4, black) shows a large seasonal cycle, of about $3.5\times10^6$ km$^2$ in both area and extent, throughout the 8-year reference experiment timeseries. This is superimposed on a smaller-amplitude year-to-year variability, predominately in the spring-through-fall ice cover, with little variability on subseasonal timescales. Simulated integral sea-ice area compares overall well to observations (green curves), capturing the expected annual freezing over of the entire model domain, as well as on average the timings of the onsets of seasonal refreezing and melting, however in most years (but 1994 & 1997) model sea-ice coverage shows a low bias at the summer-time minimum. This corresponds to a low bias in model permanent sea ice, where in observations sea ice consolidates and thickens over southwestern margins of the gyre against the Antarctic peninsula – a known bias of CORE-2 forced simulations (e.g. *Downes et al.*, 2015). Indeed, CORE-2 features too weak cold-air outbreaks, and instead generally too strong westerlies crossing the Antarctic peninsula, apporting too warm air from the west, overly melting sea ice and advecting it eastward, with an especially strong signal in summer. Such biases are typically mediated in higher-resolution reanalysis-forced simulations, for example based on ERA-I (e.g. *Dinniman et al.*, 2015).

**Water masses** An overview of simulated water masses is obtained by a 5 year (1993-1997) model volume census in conservative temperature ($\Theta$)-absolute salinity ($S_A$) space for ice-shelf cavities, as well as several regional subdomains in the open ocean.

On the southwestern Weddell Sea open-ocean continental shelf outside the FRIS cavity (shaded white on map in Fig. 5a), the model reference simulation features four major water mass poles (Fig. 5b): the relatively warm and salty (modified) warm deep water ((M)WDW), transiting along

the MWDW mixing lines into the fresh pole of winter waters (WW) at the surface freezing point. Sea-ice production and atmospheric cooling on the wide continental shelf form the third major pole, high salinity shelf waters (HSSW), characterized by $S_A$ in excess of 34.8 g kg$^{-1}$ reaching peaks above 35.1 g kg$^{-1}$. Note these are locally formed and not present on the eastern shelves, where salinities remain below 34.8 g kg$^{-1}$ (see Suppl. Fig. S1). Their interaction with FRIS basal melting at depth produces the freshened ice-shelf waters (ISW) with temperatures below the surface freezing point which, leaving the cavity, form the forth major water mass pole on the open-ocean continental shelf. Furthermore there are lighter summer-formed Antarctic surface waters (AASW), which, while occupying large extents of the $\Theta$-$S_A$ space, represent only comparatively small fractions of the continental shelf ocean volume.

The reference-experiment water masses inside the FRIS cavity are color shaded in Fig. 6 (EWIS and Larsen cavity water masses are displayed and discussed in Suppl. Fig. S2 and Suppl. Note S1). Underneath FRIS, waters above the surface freezing point represent only a small fraction of the total cavity ocean volume. Here major water masses are shown to lie below the surface freezing point along the various meltwater mixing lines describing the transformation of HSSW into ISW through ice-shelf melting (also Gade lines; *Gade*, 1979), with $\Theta$ as low as $-3.2^{\circ}$C representing melting at the deepest icedrafts. Observed summer-time sub-ice-shelf profile $\Theta$-$S_A$ from boreholes S1–S5 and F1–F4 situated in the Ronne cavity and to the south of Berkner Island, as well as from FSW1–2, FSE1–2 and FNE1–3 situated in the Filchner cavity, as mapped in Fig. 1, are displayed as black dots in comparison to the model's FRIS volumetric water mass census in Fig. 6. Observed FRIS cavity $\Theta$-$S_A$ properties are found to coincide with the major pole of FRIS ISW water masses simulated by the reference experiment. Overall the agreement between available borehole observations and model reference simulation is striking. In particular, modelled $\Theta$-$S_A$ reveal the observed presence of three poles of source water-mass types which enter the cavity with temperatures near the surface freezing point but differing salinities as witnesses of different regimes of HSSW production along the ice front. At lower temperatures, ISW collapses onto one pole elongated along the meltwater mixing line. For the lowest observed $\Theta$, borehole profiles coincide with the fresher end of the modelled pole of ISW

(in that temperature range). While the sparse observational coverage prevents a complete view of real-world water masses in the FRIS cavity, we note that sub-glacial runoff, not included in the present reference simulation, provides an additional source of freshening in the real world and may imply a somewhat salty bias in the model (e.g. *Huhn et al.*, 2018).

Outside the FRIS cavity, observed $\Theta$-$S_A$ from all available open-ocean hydrographic profiles (cf. section 2.3, mapped in Fig. 5a by green dots for profiles within the southwestern continental-shelf region considered in Fig. 5b) are superimposed on the colored model volumetric $\Theta$-$S_A$ contours in Fig. 5b by gray dots. As within the cavity, also on the open-ocean southwestern Weddell shelf, in-situ observed water-mass characteristics are strikingly consistent with those modelled. We note a bias towards slightly too fresh and cold modelled WDW, which is somewhat more pronounced on the continental shelves in front of FRIS, and EWIS, than in the deep open gyre (see Suppl. Fig. S1). For the interest of brevity we do not further describe the water-mass characteristics in all other regions of the model here, but point the interested reader to Suppl. Fig. S1 & Note S1. We note however that regional changes in water-mass characteristics associated with the production, sinking, and entrainment of bottom waters over the southwestern Weddell continental shelf and slope are consistent with observed profiles.

Corresponding maps of time-average simulated $\Theta$-$S_A$ at the sea floor are displayed in Fig. 7a,b (note that, to compare with preponderantly summer-time observational campaigns, February conditions are shown here). They reveal, at regional scale, warm and salty deep and bottom waters of the gyre that stand in stark contrast to the cold continental-shelf waters, the latter typically much closer to or even colder than the surface freezing temperature. At the continental-shelf scale, the eastern Weddell Sea continental shelf adjacing EWIS distinguishes itself as being much fresher than the shelves of the southwestern Weddell Sea adjacing FRIS and Larsen ice shelves (consistent with their classification as fresh versus dense shelves respectively, e.g. *Thompson et al.*, 2018, and references therein). The fresh eastern-shelf waters are advected southwestward following the coast onto the shelf east of the Filchner Trough. With admixture of MWDW accessing the shelf west of Brunt ice shelf, they form a warm and fresh shelf water mass reaching all the way to the eastern Filchner icefront in this 5-year February average. Several other

intrusions of MWDW crossing the shelf break deep onto the southwestern continental shelf are clearly visible in the bottom temperature field (Fig. 7a), including in the Central Trough west of Berkner bank, reaching all the way to the icefront (Fig. 7e). In the FRIS cavity, bottom waters are below the surface freezing point everywhere, decreasing below $-3°C$ near the deepest grounding lines. The saltiest waters enter the cavity in the Ronne Trough freshening on their various pathways through FRIS through admixture of ice-shelf melt waters, a transformation also clearly visible in a section below the Filchner ice shelf (Fig. 7c,d – along the green line in Fig. 7b). On the continental shelf just north of the icefront (Fig. 7e,f – section along the cyan line in Fig. 7b), waters below the surface freezing point fill the entire Ronne and Filchner Troughs in this 5-year February average, spilling above the depth of the icedraft, and with the coolest outflowing ISW at this time-of-year located on the eastern side of the Ronne and western side of the Filchner Troughs (Fig. 7e). The outflowing potentially-supercooled ISW, mixing with continental-shelf HSSW, fills the entire Filchner Trough reaching the continental shelf break around 74.5°S (Fig. 7a,c). A signature of the overflow of such dense shelf waters (ISW+HSSW) out of the Filchner Trough may be indicated by a marked gradient on the continental slope downstream of the Filchner sill (Fig. 7a), where warm and salty bottom waters transition westward towards much colder waters. In the vertical, ISW are overlaid by warmer waters (MWDW & WW), forming the characteristic V-shape at the continental shelf break (Fig. 7c,d). This V-shaped layer of MWDW and WW is itself capped by a warm and fresh seasonal thermocline of AASW, extending all the way from the open gyre across the FRIS shelf to the icefront (Fig. 7c,d). Interestingly, all the main features present in Fig. 7 and discussed in this paragraph are in very good agreement with past observational findings: MWDW intrusion pathways onto the continental shelf (e.g. *Nicholls et al.*, 2009; *Darelius et al.*, 2014, 2016; *Ryan et al.*, 2017); HSSW formation on the western Ronne continental shelf and its pathways within the cavity (e.g. *Nicholls et al.*, 2009); the V-shaped layer of MWDW and WW at the continental shelf break (e.g. *Thompson et al.*, 2018); ISW on the continental shelf and its outflow from the northwestern Filchner sill (*Foldvik*, 2004; *Daae et al.*, 2018); and the overall water-mass distribution just outside the Filchner-Ronne ice-shelf front (*Mackensen*, 2001). The two main departures of

simulated water-mass regional and vertical repartitions are: (i) the peak HSSW produced in front of western Ronne may not be quite salty enough (e.g. in one given year's summer, February 1995, in the deepest Ronne Trough, below 500 m, just outside the icefront, simulated absolute salinities exceed 34.925 g/kg, versus those observed exceed 35 g/kg, *Mackensen*, 2001, yet observational sparsity precludes a full assessment), and (ii) the surface stratification in front of FRIS seems too strong with a thus too thin, too warm and fresh surface layer (*Mackensen*, 2001).

**Circulation** The time-average model barotropic streamfunction, mapped in Fig. 8a, shows a cyclonic gyre circulation with total transports exceeding 60 Sv (a local recirculation at the gyre core near 5°W, 61°S increases this to a peak of 75 Sv). About 10–15 Sv of this are carried by coastal and slope branches. Another strong internal branch, which transports about 25 Sv roughly following the 4000 m isobath and not extending beyond 71°S, is associated with the WDW gyre recirculation that is not directly involved in water-mass modifications induced by intense cooling and sea-ice formation on the Weddell Sea continental shelves. These simulated circulations are consistent with the overall observational picture (e.g. *Schröder and Fahrbach*, 1999; *Armitage et al.*, 2018; *Reeve et al.*, 2019). In particular, the total flow in the southern branch of the gyre entering the domain from the east is, if somewhat stronger, roughly consistent with the estimates at 0°E by *Schröder and Fahrbach* (1999, 66 Sv) and *Klatt et al.* (2005, 56±8 Sv). The model annual-mean transport associated with the slope front, across ≈ 17°W, is comparable to the early-autumn 1995 estimate by *Heywood et al.* (1998) of 14 Sv. Near the northwestern gyre exit, the model boundary transport (between Joinville Island and 47.5°W), made up of several branches including coastal, slope and Weddell fronts, also compares well to the estimate by *Thompson and Heywood* (2008), totalling to 46±8Sv (with the remainder of the gyre transport occurring further east). From this predominant cyclonic gyre circulation, cyclonic incursions spin off onto the widening southwestern Weddell continental shelf. In the time-average, these are in particular the coastal current incursion onto the continental shelf east of the Filchner Trough, as well as onto the Ronne continental shelf west of Berkner Bank (Central Trough) and less far-reaching just east of Ronne Trough. Besides the major cyclonic circulation, a

smaller-amplitude anticyclonic barotropic circulation (peaks at 0.6 Sv) links the FRIS cavity and the continental shelf. It represents the overall inflow into FRIS in the Ronne Trough and outflow through the Filchner icefront with several branches/pathways, a direct outflow at the western edge of the Ronne Trough, a deep flow to the south of Korff, and in part Henry ice rises, rejoining a shallower more direct branch of the anticyclonic cavity circulation on its path around the south of Berkner Island. The latter is suggested here to also be alimented by direct inflow west of Berkner Island originating from the Berkner shelf.

The horizontal barotropic circulation is associated with a vertical circulation that can be described by the time-average meridional overturning streamfunction (Fig. 8b). Two counter-rotating cells dominate the overturning in latitude-pressure space: a counter-clockwise rotating cell mostly representative of the open-ocean gyre, and a clockwise circulation mostly representative of the ice-shelf cavity. The two cells overlap on the continental shelf. The open-gyre cell advects about 0.8 Sv of thermocline waters (WDW) from the central gyre southwards until about 72.5°S, from where a part starts to downwell and another part reaches the average shelf break further south. Above, the open-gyre cell advects an additional 0.8 Sv of lighter surface waters southward onto the continental shelf (half reaching midshelf, a quarter all the way to the ice front), where they downwell as dense shelf waters (HSSW), and are eventually exported down the continental slope northward. About 0.2–0.4 Sv of these dense continental shelf waters are not exported directly but first become associated with the cavity circulation cell, which carries them southward into the FRIS cavity, where they upwell (transformed into ISW) and move back northward following the average ice draft. The cavity cell extends northward beyond the ice front up to the continental shelf break, where cavity waters (ISW) outflow and sink at a rate of a few $O(0.1)$ Sv. Note that this meridional-depth average hides wide regional variability of a system, which is far from being zonally symmetric. So, while helpful in providing an overall idea of the vertical circulation, the meridional overturning streamfunction cannot be interpreted in terms of water-mass circulation and production.

Here, the peak 0.4 Sv FRIS volume overturning suggested by Fig. 8b, together with the net production of ice-shelf meltwater of 4.9 mSv in the reference experiment (160 Gt/yr, Table 1),

suggest a meltwater composition of the FRIS outflow, and a meltwater production efficiency of the FRIS ice and meltwater pump (used here to signify the volume of meltwater produced per volume of overturning transport into the cavity) of around 1 %. This is in agreement with the observational estimate of the glacial meltwater content in outflowing ISW (*Naveira Garabato et al.*, 2016; *Huhn et al.*, 2018).

# 4 Role of tides

In the following we examine the role of tides in setting the properties of the Weddell oceanic circulation, and of the reference experiment discussed above (in section 3), in particular in terms of ice-shelf melting, its mechanisms and attendant changes in large-scale circulation and water mass characteristics. To do so we analyze a sensitivity experiment, different from the reference experiment only by the absence of tidal boundary forcing, with otherwise the exact same initialization, boundary and atmospheric forcing, as well as the same 8-year time span of simulation 1990–1997. Discussion in comparison to previous modelling studies, in particular *Makinson et al.* (2011) and *Mueller et al.* (2018), follows in section 5.

**Tidal signal in Weddell ice-shelf melt** Timeseries of integral ice-shelf melt in the perturbation experiment without tidal boundary forcing are displayed in Fig. 2a & b (by black-edged colored symbols and black-dashed colored lines) in comparison to those of the tide-forced reference experiment discussed above (by plain colored symbols and lines). In the absence of tides, melt rates adjust from the prescribed meltrates of the forcing simulation (triangles) to the interactions with the regional higher-resolution ocean during a quick initial spinup, not discernible from seasonal and year-to-year variability beyond the first 5 days. In contrast, in the simulation with tides the major adjustment occurs over several months during the first year.

In the 5-year time-average (over simulated years 4–8, Table 1) the presence of tides enhances net basal melting in the Weddell cavities by about 50 % for both EWIS ($\Delta = 19$ Gt/yr) and FRIS (54 Gt/yr), and almost 80 % for Larsen cavities (19 Gt/yr) compared to the state without tides. In the

total over the southwestern Weddell region, tides raise ice-shelf meltwater fluxes by almost 100 Gt/yr, and thereby to a rate that roughly equals the integral iceberg melt. Note that here icebergs' trajectories and melting are prescribed and do not interact with tides. How tides may impact calving, drift and melting of Antarctic icebergs thereby remains to be assessed in dedicated future modelling configurations.

These net tidal signals are the residual of tidal impacts on both melting and freezing. The 5-year time-average maps (Fig. 3a,b) show that tides enhance the intensity of not only melting but also freezing where both occur, and thereby make simulated melt rate patterns closer to observations (Fig. 3c,d). The overall spatial pattern of melting versus freezing regions is similar in presence and in absence of tides. Regions with a change in sign of the basal mass balance from melting to freezing are rare, and include remote parts of Riiser-Larsen and Brunt-Stancomb ice shelves, as well as the refreezing patch north of the central-Ronne ice rises, which besides intensifying, somewhat expands spatially north- and westward in presence of tides. Regarding amplitude, the largest increases occur, for freezing, under central Ronne, and for melting, in the central and eastern Ronne and Filchner Troughs, over the shallow-water regions near the eastern Ronne icefront and in South Channel (south of the central Ronne ice rises, cf. Fig. 1), as well as in several spots in EWIS and Larsen located mostly, but not exclusively, near their icefronts. Integrating the two poles of melting and freezing separately over the cavities (see Table 1) shows that refreezing in presence of tides remains small underneath Larsen, and starts to become noticeable, increasing from 2 % to 6 % of the integral melt, under EWIS. For FRIS, a more than 110 Gt/yr increase in melting, representing nearly a doubling (from 136 to 248 Gt/yr), is significantly offset by 60 Gt/yr of additional refreezing, making the latter almost triple (from 31 to 89 Gt/yr). Thus, whereas refreezing is overall small under the small shallow ice shelves and remains so with tides, underneath FRIS, where it already amounts to almost a quarter of the melt (23 %) in absence of tides, it enhances to more than a third (36 %) with tides. By augmenting the net FRIS meltwater production from 3.25 to nearly 5 mSv (from 105 to 159 Gt/yr), tides thus significantly enhance the FRIS ice pump and make it closer to what is known from observations (as of the *Moholdt et al.*, 2014, estimate of a FRIS freeze/melt ratio of 77/201 $\approx$ 38 %). (Note the

term ice pump is used here, and in what follows, to signify the melt-driven cavity volume overturning circulation, with more melting driving a more vigorous cavity circulation and, in direct association, enhanced refreezing along its upward branches, e.g. *Lewis and Perkin*, 1986; *Gwyther et al.*, 2015).

Net Weddell ice-shelf basal melt rates (Fig. 2a,b) show important year-to-year variations, both in absence and in presence of tides. Whereas any significant differences are not fully characterizable from the present set of 8-year simulations, interannual variations are somewhat dampened in the absence of tides, which is especially visible for the largest simulated anomaly (the warm summer and melting peak of 1993). It is interesting to note here that, while some year-to-year anomalies differ between the three ice shelves considered here, others covary. This points to dynamical processes of different scale at play simultaneously, including both small-scale regional specificity and large-scale driving of the sub-ice shelf circulations and the tidal impact thereon. Importantly, tidal circulations are shown to enhance the integral basal melt water fluxes in all cavities of the Weddell Sea and in all months of the year. In the absence of tides, Weddell basal melt water fluxes are seen to be typically elevated in summer through autumn with a peak in early autumn. The tidal enhancement has itself a marked seasonal distribution, which tends to occur in this season of peak melting (Fig. 2a). Under FRIS, tides induce an additional secondary peak in melting in late winter (Fig. 2a).

**Mechanisms of the tidal modulation in ice-shelf melt** The mechanisms through which the presence of tides can impact ice-shelf basal melting are changes in the kinetic energy of ocean currents at the ice-shelf base and changes in the thermohaline properties of the water masses interacting with the ice shelves, the latter possibly arising through a combination of all, tide-driven changes in shelfbreak exchanges, shelf mixing, shelf-cavity exchanges, cavity pathways and cavity mixing and melting (e.g. *Padman et al.*, 2018; *Jourdain et al.*, 2019).

The signature of tides in the time-average top boundary layer (tbl) current speed $c_{tbl}$ is displayed in Fig. 9c (note, $c_{tbl}$ is obtained as the time-mean of the instantaneous absolute velocity thus including the speed of the time-mean flow as well as that of high-frequency tidal and other

currents; it pertains to the tbl in the cavities and for completeness to the top 30 m flow in the open ocean). It clearly reveals a significant tide-driven increase in kinetic energy at the base of the ice drafts in all cavities of the Weddell Sea. Whereas, in the absence of tides, tbl current speeds $c_{tbl}$ in excess of 10 cm/s occur primarily along the paths of time-mean currents (Fig. 9b), in the presence of tides (Fig. 9a) surface-layer speed is enhanced over the bulk of the Weddell continental shelves (by about 2-10 cm/s), with peak enhancements ($\geq$ 20 cm/s) on the shallower part of the continental shelves just adjacing the shelfbreak, such as to the east and to the west of the Filchner Trough, and along the southwestern corner of the Ronne shelf edge along 72°S. At the ice-shelf bases, tides enhance the tbl speed throughout. Peak enhancements of 20–30 cm/s are reached in several locations of EWIS, and the southern Larsen C. Underneath FRIS they occur within Ronne and Filchner Troughs, in several bottlenecks of the Ronne tributaries, to the north of the Ronne ice rises, and, in particular, in South Channel and along the shallow eastern Ronne ice front. The regions of enhanced tbl tidal speeds simulated here thereby correspond, both on the continental shelves and in the cavities, to the regions of maximum tidal currents (as estimated by barotropic tide models e.g. *Robertson et al.*, 1998; *Padman et al.*, 2018), and are expected to be highly sensitive to cavity geometry (e.g. *Padman et al.*, 2018; *Rosier et al.*, 2018). As a local exception, a decrease of speed surrounding Berkner Island likely reflects a tidal broadening of the Berkner Island boundary current. Importantly, this tidal enhancement of the time-average tbl speed ($\Delta c_{tbl}$, Fig. 9c) does overall *not* arise from a residual time-mean circulation change induced by tides (changes in $c_{tbl}$ associated with the 5-year mean tidally-induced circulation alternate in sign and typically do not exceed 5 cm/s in magnitude – not shown). Instead, it predominately reflects the systematic and wide-spread enhanced energy of time-varying tbl currents (zero-mean – not shown) throughout the cavities.

Fig. 9f shows overall cooling throughout the tbl of the Weddell cavities. In the absence of tides (Fig. 9e), the tbl of the shallow EWIS and Larsen cavities is typically warmer than the local freezing point ($T_b$) by 0.1-0.2 K. Also underneath FRIS the time-average reveals a surface tbl above freezing without tides, with peak temperature differences to the local freezing point ($T_{tbl} - T_b$) in excess of +0.2 K, in particular near the grounding lines. In presence of tides

(Fig. 9d) regional thermal contrasts reduce yielding a more homogeneous cavity tbl, closer to the local freezing point throughout. Warm regions, in which tides drive enhanced melting, cool with tides, and cold regions, with enhanced refreezing, warm with tides. The time-average change in cavity thermal *driving* thus predominately reflects the *response* of the tbl to the tidal input of mechanical energy.

The respective contributions of these dynamical (Fig. 9a-c) and thermohaline (Fig. 9d-f) tidal changes in the cavity tbl to the tide-induced change ($\Delta \equiv tide - notide$) in ice-shelf basal melting $\mathcal{M}$ ($< 0$ melt) can be quantified as (cf. *Jourdain et al.*, 2019)

$$\begin{aligned} -\Delta\mathcal{M} &\approx \Delta\left(Q_{tbl}/L_{fi}\right) = \Delta\left(\alpha c_{tbl}\left(T_{tbl}-T_b\right)\right) \\ &= \alpha\Delta c_{tbl}\left(T_{tbl}-T_b\right)\big|_{no} + \alpha c_{tbl}\big|_{no}\,\Delta\left(T_{tbl}-T_b\right) + \alpha\Delta c_{tbl}\Delta\left(T_{tbl}-T_b\right) \\ &= -\left(\Delta\mathcal{M}_{DYN} + \Delta\mathcal{M}_{THERM} + \Delta\mathcal{M}_{COV}\right), \end{aligned} \tag{2}$$

where we have used that $Q_{tbl}$, given by eq. (1), is directly proportional to $\mathcal{M}$ when neglecting heat diffusion into the ice, we introduced $\alpha \equiv \left(\rho_w c_{pw} St_T\right)/L_{fi}$ with $L_{fi}$ the latent heat of fusion of ice, and $\big|_{no}$ denotes the cavity state without tides. In the resulting decomposition of tide-driven basal melt $\Delta\mathcal{M}$, the dynamical contribution $\Delta\mathcal{M}_{DYN}$ reflects a stronger ocean-ice heat flux due to tide-induced tbl kinetic energy ($\Delta c_{tbl}$, Fig. 9c). Thermodynamical ($\Delta\mathcal{M}_{THERM}$) and covariational ($\Delta\mathcal{M}_{COV}$) components, in turn, reflect tide-induced changes in tbl temperature ($\Delta\left(T_{tbl}-T_b\right)$, Fig. 9f), which either arise in phase with the tidal enhancement of tbl kinetic energy ($\Delta\mathcal{M}_{COV}$), or not ($\Delta\mathcal{M}_{THERM}$). Here $\Delta\mathcal{M}_{THERM}$ is expected to dominate where tide-induced warming occurs unrelated to dynamical changes (such as when advected from the continental shelves) or for a vigorous cavity circulation that quickly evacuates cold meltwater from regions of melting (such as in warm cavities *Jourdain et al.*, 2019). $\Delta\mathcal{M}_{COV}$, to the contrary, may dominate where increased tbl kinetic energy produces cold meltwater that is not quickly exported away (such as in more sluggish cold cavities).

Timeseries of the tidal signal in ice-shelf melt $\Delta\mathcal{M}(t)$ for the Weddell domain, that is the difference between tidal and non-tidal integral melting from Fig. 2b, are displayed in Fig. 9g, together with the timeseries of the three mechanistic contributions given by Eq. (2). Here the

approximation in Eq. (2) is confirmed to be minor, with the sum of the three contributions (gray dash in Fig. 9g) reproducing near exactly the total change of melt (black in Fig. 9g). The tide-driven melt ($\Delta\mathcal{M}$, black, $< 0$ more melt) oscillates, after the initial spin up, seasonally and from year to year, at $\approx$ 100 Gt/yr in the Weddell total, and is shown to be solely generated by an about 8 times larger dynamical enhancement ($\Delta\mathcal{M}_{DYN}$, green), which drives all the seasonal and interannual variations of the tidal enhancement, and in absence of thermal responses of the cavity would reflect the net change seen. The tbl however responds thermally to this mechanical driving, mostly at zero time lag (captured by the covariational term, $\Delta\mathcal{M}_{COV}$, cyan), cooling at times of enhanced melting and cold ISW production. Together with a smaller non-instantaneous thermal response ($\Delta\mathcal{M}_{THERM}$, blue) of $\approx$ 100 Gt/yr, the net thermal response ($\Delta\mathcal{M}_{COV} + \Delta\mathcal{M}_{THERM}$) thereby substantially limits the net effect of tides enhancing Weddell ice-shelf melt. This decomposition holds for each individual of the three ice-shelf formations, each showing a very similar repartition into the different mechanistic contributions to the tide-driven basal melting, as further quantified for the 5-year time average in Table 2: The tidal increase in kinetic energy at the ice-shelf bases alone enhances melt by around 130 Gt/yr for EWIS and Larsen, and nearly 500 Gt/yr for FRIS. Thermal adjustments, 82.5-85 % of which occur at zero-lag (covariational), limit the tide-driven enhancement to the simulated $\approx$ 20 Gt/yr for the former and 54 Gt/yr for the latter.

**Further implications of tides in the Weddell Sea** Here we briefly focus on integral, barotropic & overturning, metrics of tide-driven changes in the mean flow, which can reflect both dynamical (e.g. *Bessières et al.*, 2008; *Padman et al.*, 2018; *Jourdain et al.*, 2019) and melt-induced (e.g. *Jourdain et al.*, 2019) tidal residual circulations, the latter driven by the tidal imprints on ice-shelf melting discussed above. Figure 8 maps these tidal signals (in panels e & f respectively) and also compares their time-average states with (a & b) and without (c & d) tides.

Regarding the barotropic circulation (Fig. 8a,c,e), tide-induced changes in the open gyre are small relative to the total transport (typically less than 5 %), with the strength of the cyclonic gyre excursions onto the continental shelves, to the east of Filchner and Ronne Troughs as well as onto

the Larsen shelf, somewhat reduced in presence of tides. The most significant signal, in terms of relative change, is an enhancement of the predominately anticyclonic barotropic gyre circulation within the FRIS cavity, by around 0.1 Sv of 0.2–0.4 Sv. In association, several local changes in pathways are found, especially in the Ronne local cross ice-front circulation, which becomes more anticyclonic, as well as in remote parts of Ronne and in the Filchner Trough.

As to the overturning circulation (Fig. 8b,d,f), tides induce changes in both of its cells, the counterclockwise open-gyre and the clockwise cavity cell. The open-gyre cell weakens at depth, by 0.4 of 2 Sv, or by 20 %. In the upper 500 m, local changes suggest it reaches closer to the surface around 72°S (the latitude of enhanced southwestern shelf break tidal kinetic energy, cf. Fig. 9a,c) and its extension onto the southwestern continental shelf somewhat weakens at mid-shelf, while its furthest extension towards the southern ice fronts instead somewhat intensifies. The most pronounced relative change, again, occurs in the sub-ice-shelf cavities: here the cavity cell, associated to the transformation of HSSW into ISW through ice-shelf melt interactions, shows a marked tide-induced increase almost doubling from peaks at 0.2 to 0.4 Sv near the FRIS ice fronts, and from 0.1 to 0.2 Sv in more remote parts of the FRIS cavity, reflecting a tide-induced enhancement of the FRIS ice pump. It is worth noting here that this enhancement of the mean FRIS circulation is not strong enough to account for the simulated enhancement of tbl flow speed associated with enhanced melting, and the mechanical energy input is instead provided by energized time-variable (tidal) currents. While these integral overturning metrics are useful to highlight such important basic mechanistic understanding, they are unsatisfactory to document water-mass circulations, and so we do not further investigate this aspect here. We note however that by nearly doubling the circulation in the cavity, and therefore substantially enhancing the associated production of ISW, tides may have a direct impact on the characteristics of bottom waters.

Here a first insight into such tidal impacts on water-mass characteristics in the Weddell ice-shelf cavities and the adjacent continental shelves is gained from volumetric water-mass differences in the $\Theta$-$S_A$ space (cf. Suppl. Fig. S3, and for a more detailed description Suppl. Note S1). Whereas overall changes, especially in the open ocean, are weak and fragmented, the several more

pronounced and systematic tide-induced water-mass changes that stand out are indicative of being a response to the tide-driven enhancement of ice-shelf melting and the associated cooling and freshening. In cavity, shelf and open ocean, these are the following. (I) In the FRIS cavity, the volume of waters above the surface freezing point is reduced and that of sub-freezing point waters increased (also for EWIS), with overall (besides multiple localized poles of changes in the $\Theta$-$S_A$ space) more volume in the fresher varieties of FRIS ISW in presence of tides. (II) The ISW outflowing from FRIS onto the continental shelf show a clear signature of decrease in its saltiest and increase in its freshest varieties. (Other changes on the continental shelf are a reduction of saltiest waters along the dense-shelf water/MWDW mixing line, as well as overall more shelf-produced HSSW, and, for the EWIS open-shelf, more outflowing sub-surface freezing point waters). (III) In the off-shelf deep open ocean, a sole marked water-mass change induced by the presence of tides stands out: a freshening of the densest (deep and bottom) water masses in the western Weddell Sea. This water mass is produced locally through southwestern Weddell shelf and cavity processes (it is not present in the eastern gyre), and the changes in its properties thus reflect the signature of tides on Weddell ocean–ice-shelf interactions and the outflowing shelf water-mass properties.

The tide-induced enhancement of ISW outflow (Figs. 2, 8f, S3) may be furthermore anticipated to impact the continental shelf stratification and accordingly its sea-ice cover. Such tide-driven changes in sea-ice volume in the southwestern Weddell Sea are quantified in Fig. 10. Sea-ice volume on the southwestern Weddell Sea continental shelf is enhanced in all months of the year (Fig. 10b), by about 5 %. Given that tides do not systematically impact area coverage (see Fig. 4 for Weddell integrals, mapped concentrations also do not show any marked large-scale changes – not shown), this reflects a tidal impact on the thickness of sea ice (actual thickness, not ice volume per unit area). Thickness increases by on average 5 cm on top of a seasonally-varying continental shelf sea-ice thickness of 1–2 m, and the peak enhancement of 10 cm occurs during the season of thickest ice in summer (mapped in Fig. 10a). Rather than reflecting a local tidal signature on for example shelf mixing, here we suggest that this tidal imprint on continental-shelf sea-ice volume passes via tide–ocean–ice-shelf interactions in Weddell cavities through the tidal

enhancement of glacial freshwater production and export enhancing shelf stratification. This mechanism is consistent with previous circumpolar models reporting Weddell sea-ice thickening in response to enhanced meltwater forcing (e.g. *Merino et al.*, 2018). In particular, results by *Hellmer* (2004) of a 100 % meltwater addition, from opening ice-shelf cavities, leading to a 20 cm sea-ice thickening (about 10–20 %) are comparable, also in magnitude, to present results of a 50 % meltwater enhancement, here tide-driven, leading to a 10 cm thickening (about 5-10%).

# 5 Discussion

We have presented a first assessment of tide-induced changes in Weddell Sea ocean–ice-shelf interactions in realistic simulations of the southwestern Weddell Sea gyre – continental-shelf – cavity system forced with interannually-varying atmospheric and ocean-boundary conditions. Previous modelling assessments of the tidal impact on FRIS ice-shelf melting have considered solutions (i) to homogeneous and constant FRIS continental-shelf forcing (*Mueller et al.*, 2018) in cold and warm shelf conditions, and (ii) to climatological ocean forcing in combination with spatially-heterogeneous seasonally-modulated FRIS continental-shelf surface thermohaline relaxation (*Makinson et al.*, 2011). Both used ocean-only simulations (no sea ice) across relatively-focussed regional domains (not extending much beyond the continental shelf break and not including other Weddell Sea cavities) at horizontal resolutions coarser than in the present study (2.5 – 4 times).

In comparison to *Makinson et al.* (2011)'s results, simulations analyzed here suggest a smaller *relative* net enhancement of FRIS basal melt fluxes in response to tides. In magnitude, tide-induced changes of the FRIS ice pump however closely agree between the two studies, in terms of both net melt and basal melt-to-freeze ratios (Makinson's FRIS net increase of 50 Gt/yr reflecting a ratio of changes in freezing versus melting, $\Delta$freeze/$\Delta$melt, of 53.3 %, compared to this study's net increase of 54 Gt/yr reflecting a ratio of 51.6 %). In the present study, these tide-induced changes act on a larger non-tidal net melt (105 Gt/yr here versus 41 Gt/yr in *Makinson et al.*, 2011), and this implies that here the net tide-driven change reflects a 50 %

increase (compared to the 100 % increase obtained by Makinson), and similarly that here changes in refreezing and melting are $\leq$3-fold and $\leq$2-fold (compared to 6-fold and 3-fold in their study). The spatial patterns of non-tidal and tidal FRIS melt rates are also overall similar between the two studies.

In contrast, results of this study differ from the homogeneous-shelf condition-forced FRIS ocean-tide modelling results by *Mueller et al.* (2018) in terms of both the non-tidal background and the tide-driven changes, in all the net signal, the ice pump as reflected by the refreezing-to-melt ratio, as well as the spatial distribution of freezing and melting regions. This is to be expected given that the thermohaline-forced west-to-east anticyclonic cavity circulation is absent (in *Mueller et al.*, 2018), a circulation suggested by available observations, simulated in this study as well as in *Makinson et al.* (2011), and likely to represent the dominant contribution to the cavity mean flow especially within Ronne & Filchner Troughs, where tidal residuals are estimated to contribute less than 10% (*Makinson and Nicholls*, 1999). Under the uniform thermohaline shelf forcing of *Mueller et al.* (2018) and the associated east-to-west cyclonic cavity circulation, the absence of Ronne inflows leads to widespread refreezing over the majority of the Ronne sector of FRIS. The latter is a likely reason for the near-compensating tidal increases in melting and refreezing, and the near-zero tidal signal in the net FRIS basal mass balance, obtained by *Mueller et al.* (2018). In this context, it is interesting to note that several of the tide-induced changes in FRIS circulation patterns obtained here in full tide–ocean–ice-shelf interactions agree with the tide-only results obtained in FRIS barotropic experiments by *Makinson and Nicholls* (1999), including tide-driven changes in the eastern Ronne cross-icefront transports, an enhancement of the anticyclonic circulation around Berkner Island as well as a reduction in eastward transport through South Channel (Fig. 8e). Similarly, there are also similarities to the constant thermohaline and tide-forced results of *Mueller et al.* (2018), and they include enhanced melting in the shallow South Channel and western Ronne icefront, mid-Ronne enhanced freezing and a predominately mechanical driving of the integral tide-induced changes.

This study provides an assessment of the dynamical and thermodynamical mechanisms at play in ice-shelf cavities' top boundary layer associated with tide-induced melt, for FRIS and other

Weddell Sea ice-shelf cavities, and under realistic thermohaline forcing scenarios. For the Amundsen Sea, a previous realistic-simulation assessment (*Jourdain et al.*, 2019) finds a mechanistically comparable tidal impact: in both cases, top boundary-layer thermodynamic adjustment diminishes the mechanical tidal driving of increased melt. Interestingly, in the cold Weddell Sea cavities assessed here, in which thermal forcing of ice-shelf melting is weak in the first place, the thermal adjustment response is found to be more pronounced (compensating dynamical tidal forcing to about 85-90 %) than in the warm Amundsen Sea cavities (about 40 %). Results presented here, consistent with *Jourdain et al.* (2019), suggest that the nature of the tidal signature on melt is primarily local, associated with enhanced kinetic energy at the icedraft, with the thermal top boundary layer signature reflecting the response to this mechanical enhancement of ocean–ice-shelf interactions, rather than being induced advectively by tidal residual circulations. Here it is worth to note that the heat lost from the top boundary layer through increased kinetic energy locally enhancing melt, must be reflected by tbl cooling or, especially in the case of a cold cavity characterized by limited heat available for melting ice, be replenished by heat entering the cavity. A detailed analysis of cavity heat budgets and their responses to tides remains a topic of interest for future study in this regard. Here we simply note that any required enhanced cross-icefront heat transport may reflect local changes in water-mass properties and advective pathways induced by tides independently of their interaction with ice-shelf melting, but it may also arise as a direct response to the tide-induced melting via melt-induced changes in cavity overturning and in the water masses exported, such as those reported here.

Critical-latitude effects and internal tide generation through tidal interactions with topography and ocean stratification, as well as its seasonal modulation, are all to some extent included in the presented simulations and known to contribute importantly to shape distributions of tidal energy (e.g. *Robertson*, 2001a,b; *Makinson et al.*, 2006; *Semper and Darelius*, 2017). While this study has focussed on assessing the integrated tidal impact, including these effects, on ocean-ice-shelf interactions and associated water mass pathways and transformations, further differentiating their individual contributions would provide interesting refinements to the present analysis. Analysis presented here, noting sensitivity to uncertainties, discretization and errors in cavity geometry

(e.g. *Rosier et al.*, 2018; *Padman et al.*, 2018, and references therein), also points towards the role of tides in the renewal of FRIS water masses (cf. also Suppl. Note S1 for further discussion of this aspect). In this regard it is worth to mention that a faster cavity flushing timescale would diminish the effective ocean thermal adjustment, and therefore strengthen the tidal enhancements of both ice-shelf melting and freezing where they occur, and thus, given the respective weights of the latter established here, strengthen the tide-driven net melting and meltwater production. This suggests a critical role of both cavity vertical mixing and the top boundary layer heat budget in the ice-shelf melt response to tides (e.g. *Gwyther et al.*, 2015), which points to the latter's likely sensitivity to the parameterizations employed, and in particular to the bulk parameterization of ice-shelf melt rates (and its known limitations, e.g. *Asay-Davis et al.*, 2017). Important outstanding advances thus include improved observational constraints for or elimination of remaining largely-unconstrained parameters in the bulk melt parameterization (such as Stanton numbers and especially boundary layer depth, e.g. *Jourdain et al.*, 2017), and the representations of upward sedimenting frazil-ice platelets freezing throughout the water column (e.g. *Bombosch and Jenkins*, 1995; *Smedsrud and Jenkins*, 2004; *Galton-Fenzi et al.*, 2012) as well as dynamical feedbacks between tides, ocean circulation, ice-shelf melting and water & ice depths as accessible in ocean–ice-sheet coupled simulations (e.g. *Mueller et al.*, 2018; *Reese et al.*, 2018; *Timmermann and Goeller*, 2017).

This study provides a carefully-designed high-resolution regional-model configuration capturing relevant high-latitude ocean-cryosphere processes whose simulations given their high computational cost are necessarily rather short. Given the expected long exchange timescale of the large FRIS cavity (based on the simulated circulations in Fig. 8 we obtain a rough scaling estimate of $\approx$ 13 years; observational studies using oceanographic and isotopic constraints have estimated between 4–10 years, cf. *Nicholls and Østerhus*, 2004; *Huhn et al.*, 2018), here we therefore rely on a spin-up of cavity water masses obtained in the global boundary-forcing simulation GO7, which as described in section 2 uses an overall very similar set up as the regional simulations here except its lower resolution and absence of explicit tides. Departing with thus already physically-consistent states including in cavities, regional-simulation integral

ice-shelf melt (Fig. 2), as well as integral temperature and salinity of both open and cavity ocean (not shown), do not show any adjustment processes that can be differentiated from year-to-year variability beyond their first 1-2 years. In contrast, initialization from available ocean reanalyses, which to date typically end in walls either at the entrance of cavities or at fixed latitudes cutting through continental shelves, necessarily implies extrapolation of attendant biased temperature-salinity properties far into cavities and thus demands long regional-simulation spin-ups before physically consistent water mass properties can be established. This, together with the risk that initiating with too warm continental shelf temperatures may trigger irreversibly warm states in the FRIS system (*Hellmer et al.*, 2017), has motivated our choice to not constrain the present reference experiment with reanalyses. We hope that regional high-resolution results produced and presented here may provide a useful benchmark, as further model developments will allow to partially parameterize the now known-to-be important high-latitude cryospheric processes, in cavities and shelves and in interaction with tides, in lower-resolution climate-type model simulations thereby allowing for long and regionally-unconstrained integrations. Model intercomparison studies (building on e.g. *Naughten et al.*, 2018b) between different types of high-resolution regional, lower-resolution resolved-cavity circumpolar, and global simulations with partially-parameterized processes, will thereby be of immense value to further understanding of relevant processes and systems' variability.

# 6 Conclusions

The present study assesses for the first time the impact of tides on Weddell Sea ocean–ice-shelf interactions in a coupled ocean–sea-ice model with realistic interannually-varying boundary and atmospheric forcing, fully representing two-way exchanges between the southwestern Weddell Sea open-ocean gyre, its continental shelves and ice-shelf cavities, and at higher spatial resolution than in previous ocean-only simulations with steady (*Mueller et al.*, 2018) or idealized climatological forcing (*Makinson et al.*, 2011).

In comparison to the observed Weddell Sea system, as far as known, overall circulation and water

mass features in all its three components, deep, shelf and cavity oceans, are well represented in the simulations assessed here. A key bias is a too warm summer surface layer with a too strongly stratified summer seasonal thermocline and associated low bias in summer sea-ice coverage, especially on the southwestern Weddell shelf. Nonetheless key dense shelf water masses produced by local atmosphere–ocean–tide–sea-ice–ice-shelf interactions are overall well represented. Warm Deep Water intrusions onto the continental shelves are also simulated where observed (with a seasonal and year-to-year variability that has not been fully presented here), although possibly slightly too modified (cooled & also freshened) compared to observations as they reach the remote FRIS continental shelf and its icefronts.

Key results are as follows:

- Net basal meltwater fluxes show substantial variability in all Weddell Sea ice-shelf cavities on all simulated timescales, including tidal, seasonal and year-to-year periods, where the latter are presented here for the first time in simulations of the region including tides and are suggested slightly amplified in presence of tides.

- Tides drive an increase in time-average net ice-shelf basal melt by 50 % in EWIS (+19 Gt/yr melting) and FRIS (+54 Gt/yr) and 80 % in Larsen cavities (+19 Gt/yr). Whereas refreezing is small under the small shallow ice shelves, it amounts to a quarter of melting underneath FRIS, and increases to more than a third with tides, a ratio comparable to observations (*Moholdt et al.*, 2014). This reflects a tide-driven intensification of the existing pattern of basal melting and refreezing (with integral increases in freezing reaching about 50% those in melting) and of the underlying FRIS sub-ice-shelf circulation, in terms of both the primarily anticyclonic main barotropic gyre circulation (although there is local structure, e.g. a reduction through South Channel reflecting a more cyclonic circulation there) and, especially, the cavity volume overturning circulation.

- Tide-induced changes in FRIS ocean–ice-shelf interactions and ice pump closely match the coarser-resolution isopycnal-model idealized-forcing one-year-average results obtained by the only previous FRIS ocean-tide modelling study including a representation of the

(observed) continental-shelf thermal gradients (*Makinson et al.*, 2011). Simulated FRIS basal melt patterns are also overall similar, with the main difference being refreezing outflows reaching the mid-Ronne icefront in the former study, where simulations here instead feature a narrow western-boundary outflow feature in the Ronne Trough and melt conditions all along the Ronne icefront to the east, implying somewhat different circulation regimes in the Ronne cavity.

- The tide-induced increase in Weddell ice-shelf melting is associated, both in its mean and its time-variability, with a tidal enhancement in the kinetic energy of time-varying ocean currents at the ice base, which mechanically raise the heat exchanged across the background (non-tidal) thermal gradient between the ocean–sub-ice-shelf boundary layer and the ice shelf. Tide-induced changes in this thermal gradient act to significantly damp (rather than enhance) the mechanically-induced tidal enhancement of melting (by 85-90 %, depending on cavity), since they reflect on average a response to the latter, with cooling in regions of enhanced melting and warming in regions of enhanced refreezing – a response which is to more than 80 % instantaneous, the remainder being not zero-lag correlated, inducing a slight lag to this thermal damping. The net tidal enhancement of melting may be sustained by a transition to a cooler cavity state and by tide-driven increases in heat transport into the cavity. The latter, while a detailed assessment of cavity heat budgets' sensitivity to tides is subject to future study, may be achieved, both, independently of melt through local changes of properties and their advective pathways into the cavity, and, in response to tide-induced melting through the melt-induced circulation and water-mass changes described in this study.

- Changes attendant to the tidal enhancement of FRIS basal meltwater production and cavity circulation include a slight shift towards a fresher ISW exported onto the southwestern Weddell Sea continental shelf, and a freshening and lightening of the densest deep water masses in the open gyre produced in response to the downwelling dense shelf waters, as well as a year-round increase in southwestern shelf sea-ice volume (by 5–10 %). Further refinement of diagnostics is necessary to quantify more reliably the integral tidal

contributions to the water-mass circulation in terms of transformation rates and exchanges across shelfbreak and icefronts.

**Acknowledgments**

The project was funded by the European Research Council (ERC) under the European Union's Horizon 2020 research and innovation program (grant agreement 637770), and received a GENCI grant (DARI A0020107451) for high-performance computing at IDRIS. N. J. was supported by the TROIS AS project (ANR-15-CE01-0005-01). The NEMO 3.6 & LIM3 model code is freely available at www.nemo-ocean.eu. Here we use the development branch dev_v3_6_STABLE_r6506_AGRIF_LIM3. Model customizations and parameter choices required to run the experiments presented in this paper are provided at https://doi.org/10.5281/zenodo.3384022. Observational data used in this study are publicly available as indicated in section 2.

# References

Årthun, M., P. R. Holland, K. W. Nicholls, and D. L. Feltham (2013), Eddy-Driven Exchange between the Open Ocean and a Sub–Ice Shelf Cavity, *Journal of Physical Oceanography*, *43*(11), 2372–2387, doi:10.1175/JPO-D-13-0137.1.

Adcroft, A., and J.-M. Campin (2004), Re-scaled height coordinates for accurate representation of free-surface flows in ocean circulation models, *Ocean Modelling*, *7*, 269–284, doi:10.1016/j.ocemod.2003.09.003.

Armitage, T. W. K., R. Kwok, A. F. Thompson, and G. Cunningham (2018), Dynamic Topography and Sea Level Anomalies of the Southern Ocean: Variability and Teleconnections, *Journal of Geophysical Research: Oceans*, *123*(1), 613–630, doi:10.1002/2017JC013534.

Asay-Davis, X. S., N. C. Jourdain, and Y. Nakayama (2017), Developments in Simulating and

Parameterizing Interactions Between the Southern Ocean and the Antarctic Ice Sheet, *Current Climate Change Reports*, *3*(4), 316–329, doi:10.1007/s40641-017-0071-0.

Beckmann, A., H. H. Hellmer, and R. Timmermann (1999), A numerical model of the Weddell Sea: Large-scale circulation and water mass distribution, *Journal of Geophysical Research: Oceans*, *104*(C10), 23,375–23,391, doi:10.1029/1999JC900194.

Bessières, L., G. Madec, and F. Lyard (2008), Global tidal residual mean circulation: Does it affect a climate OGCM?, *Geophysical Research Letters*, *35*(3), doi:10.1029/2007GL032644.

Bombosch, A., and A. Jenkins (1995), Modeling the formation and deposition of frazil ice beneath Filchner-Ronne Ice Shelf, *Journal of Geophysical Research*, *100*(C4), 6983, doi:10.1029/94JC03224.

Bronselaer, B., M. Winton, S. M. Griffies, W. J. Hurlin, K. B. Rodgers, O. V. Sergienko, R. J. Stouffer, and J. L. Russell (2018), Change in future climate due to Antarctic meltwater, *Nature*, *564*(7734), 53–58, doi:10.1038/s41586-018-0712-z.

Carrère, L., F. Lyard, M. Cancet, A. Guillot, and L. Roblou (2012), Fes2012: a new global tidal model taking advantage of nearly 20 years of altimetry, *Proceedings of the 20 Years of Progress in Radar Altimetry Symposium, Venice*, pp. 1–20.

Comiso, J. C. (2000, updated 2015), Bootstrap sea ice concentrations from Nimbus-7 SMMR and DMSP SSM/I-SSMIS, version 2, *Boulder, Colorado USA. NASA National Snow and Ice Data Center Distributed Active Archive Center. [Accessed March 9 2015]*, doi:10.5067/J6JQLS9EJ5HU.

Daae, K., E. Darelius, I. Fer, S. Østerhus, and S. Ryan (2018), Wind Stress Mediated Variability of the Filchner Trough Overflow, Weddell Sea, *Journal of Geophysical Research: Oceans*, doi:10.1002/2017JC013579.

Dansereau, V., P. Heimbach, and M. Losch (2014), Simulation of subice shelf melt rates in a general circulation model: Velocity-dependent transfer and the role of friction: Ice

Shelf-Ocean Interactions in a GCM, *Journal of Geophysical Research: Oceans*, *119*(3), 1765–1790, doi:10.1002/2013JC008846.

Darelius, E., K. Makinson, K. Daae, I. Fer, P. R. Holland, and K. W. Nicholls (2014), Hydrography and circulation in the Filchner Depression, Weddell Sea, Antarctica, *Journal of Geophysical Research: Oceans*, *119*(9), 5797–5814, doi:10.1002/2014JC010225.

Darelius, E., I. Fer, and K. W. Nicholls (2016), Observed vulnerability of Filchner-Ronne Ice Shelf to wind-driven inflow of warm deep water, *Nature Communications*, *7*, 12,300, doi:10.1038/ncomms12300.

Depoorter, M. A., J. L. Bamber, J. A. Griggs, J. T. M. Lenaerts, S. R. M. Ligtenberg, M. R. van den Broeke, and G. Moholdt (2013), Calving fluxes and basal melt rates of Antarctic ice shelves, *Nature*, *502*(7469), 89–92, doi:10.1038/nature12567.

Dinniman, M., X. Asay-Davis, B. Galton-Fenzi, P. Holland, A. Jenkins, and R. Timmermann (2016), Modeling Ice Shelf/Ocean Interaction in Antarctica: A Review, *Oceanography*, *29*(4), 144–153, doi:10.5670/oceanog.2016.106.

Dinniman, M. S., J. M. Klinck, L.-S. Bai, D. H. Bromwich, K. M. Hines, and D. M. Holland (2015), The Effect of Atmospheric Forcing Resolution on Delivery of Ocean Heat to the Antarctic Floating Ice Shelves, *Journal of Climate*, *28*(15), 6067–6085, doi:10.1175/JCLI-D-14-00374.1.

Downes, S., R. Farneti, P. Uotila, S. M. Griffies, S. J. Marsland, D. Bailey, E. Behrens, M. Bentsen, D. Bi, A. Biastoch, C. Böning, A. Bozec, V. M. Canuto, E. Chassignet, G. Danabasoglu, S. D. adn N. Diansky, H. Drange, P. G. Fogli, A. Gusev, A. Howard, M. Ilicak, T. Jung, M. Kelley, W. G. Large, A. Leboissetier, M. Long, J. Lu, S. Masina, A. Mishra, A. Navarra, G. Nurser, L. Patara, B. L. Samuels, D. Siorenko, P. Spence, H. Tsujino, Q. Wang, and S. G. Yeager (2015), An assessment of Southern Ocean water masses and sea ice during 1988–2007 in a suite of interannual CORE-II simulations, *Ocean Modelling*, *94*, 67–94.

Foldvik, A. (2004), Ice shelf water overflow and bottom water formation in the southern Weddell Sea, *Journal of Geophysical Research*, *109*(C2), doi:10.1029/2003JC002008.

Foldvik, A., J. H. Middleton, and T. D. Foster (1990), The tides of the southern Weddell Sea, *Deep Sea Research Part A. Oceanographic Research Papers*, *37*(8), 1345–1362, doi:10.1016/0198-0149(90)90047-Y.

Fox-Kemper, B., G. Danabasoglu, R. Ferrari, S. Griffies, R. Hallberg, M. Holland, M. Maltrud, S. Peacock, and B. Samuels (2011), Parameterization of mixed layer eddies. III: Implementation and impact in global ocean climate simulations, *Ocean Modelling*, *39*(1-2), 61–78, doi:10.1016/j.ocemod.2010.09.002.

Gade, H. G. (1979), Melting of Ice in Sea Water: A Primitive Model with Application to the Antarctic Ice Shelf and Icebergs, *Journal of Physical Oceanography*, *9*(1), 189–198, doi:10.1175/1520-0485(1979)009⟨0189:MOIISW⟩2.0.CO;2.

Galton-Fenzi, B. K., J. R. Hunter, R. Coleman, S. J. Marsland, and R. C. Warner (2012), Modeling the basal melting and marine ice accretion of the Amery Ice Shelf: MODELING MELTING & MARINE ICE ACCRETION, *Journal of Geophysical Research: Oceans*, *117*(C9), n/a–n/a, doi:10.1029/2012JC008214.

Gerdes, R., J. Determann, and K. Grosfeld (1999), Ocean circulation beneath Filchner-Ronne Ice Shelf from three-dimensional model results, *Journal of Geophysical Research: Oceans*, *104*(C7), 15,827–15,842, doi:10.1029/1999JC900053.

Golledge, N. R., E. D. Keller, N. Gomez, K. A. Naughten, J. Bernales, L. D. Trusel, and T. L. Edwards (2019), Global environmental consequences of twenty-first-century ice-sheet melt, *Nature*, *566*(7742), 65–72, doi:10.1038/s41586-019-0889-9.

Good, S. A., M. Martin, and N. A. Rayner (2013), EN4: quality controlled ocean temperature and salinity profiles and monthly objective analyses with uncertainty estimates, *J. Geophys. Res. Oceans*, *118*, 6704–6716, doi:10.1002/2013JC009067.

Gouretski, V. V., and A. I. Danilov (1993), Weddell Gyre: Structure of the eastern boundary, *Deep Sea Research Part I: Oceanographic Research Papers*, *40*(3), 561–582, doi:10.1016/0967-0637(93)90146-T.

Gwyther, D. E., B. K. Galton-Fenzi, M. S. Dinniman, J. L. Roberts, and J. R. Hunter (2015), The effect of basal friction on melting and freezing in ice shelf–ocean models, *Ocean Modelling*, *95*, 38–52, doi:10.1016/j.ocemod.2015.09.004.

Hallberg, R. (2013), Using a resolution function to regulate parameterizations of oceanic mesoscale eddy effects, *Ocean Modelling*, *72*, 92–103, doi:10.1016/j.ocemod.2013.08.007.

Hellmer, H., and D. Olbers (1989), A two-dimensional model for the thermohaline circulation under an ice shelf, *Antarctic Science*, *1*(04), doi:10.1017/S0954102089000490.

Hellmer, H. H. (2004), Impact of Antarctic ice shelf basal melting on sea ice and deep ocean properties: ANTARCTIC ICE SHELF BASAL MELTING, *Geophysical Research Letters*, *31*(L10307), doi:10.1029/2004GL019506.

Hellmer, H. H., F. Kauker, R. Timmermann, J. Determann, and J. Rae (2012), Twenty-first-century warming of a large Antarctic ice-shelf cavity by a redirected coastal current, *Nature*, *485*(7397), 225–228, doi:10.1038/nature11064.

Hellmer, H. H., F. Kauker, R. Timmermann, and T. Hattermann (2017), The Fate of the Southern Weddell Sea Continental Shelf in a Warming Climate, *Journal of Climate*, *30*(12), 4337–4350, doi:10.1175/JCLI-D-16-0420.1.

Heywood, K. J. (2004), On the fate of the Antarctic Slope Front and the origin of the Weddell Front, *Journal of Geophysical Research*, *109*(C6), doi:10.1029/2003JC002053.

Heywood, K. J., R. A. Locarnini, R. D. Frew, P. F. Dennis, and B. A. King (1998), Transport and water masses of the Antarctic Slope Front system in the eastern Weddell Sea, *Ocean, Ice and Atmosphere: Interactions at the Antarctic Continental Margin, S. S. Jacobs and R. F. Weiss, Eds., Amer. Geophys. Union*, *75*, 203–214, doi:10.1016/j.dsr.2008.06.001.

Holland, D. M., and A. Jenkins (1999), Modeling Thermodynamic Ice–Ocean Interactions at the Base of an Ice Shelf, *Journal of Physical Oceanography*, *29*(8), 1787–1800, doi:10.1175/1520-0485(1999)029⟨1787:MTIOIA⟩2.0.CO;2.

Huhn, O., T. Hattermann, P. E. D. Davis, E. Dunker, H. H. Hellmer, K. W. Nicholls, S. Østerhus, M. Rhein, M. Schröder, and J. Sültenfuß(2018), Basal Melt and Freezing Rates From First Noble Gas Samples Beneath an Ice Shelf, *Geophysical Research Letters*, doi:10.1029/2018GL079706.

IOC, SCOR, and IAPSO (2010), The international thermodynamic equation of seawater - 2010 : Calculation and use of thermodynamic properties., *Tech. rep., Intergovernmental Oceanographic Commission*.

Jenkins, A. (2004), Seasonal ventilation of the cavity beneath Filchner-Ronne Ice Shelf simulated with an isopycnic coordinate ocean model, *Journal of Geophysical Research*, *109*(C1), doi:10.1029/2001JC001086.

Jenkins, A. (2016), A Simple Model of the Ice Shelf–Ocean Boundary Layer and Current, *Journal of Physical Oceanography*, *46*(6), 1785–1803, doi:10.1175/JPO-D-15-0194.1.

Jenkins, A., and D. M. Holland (2002), A model study of ocean circulation beneath Filchner-Ronne Ice Shelf, Antarctica: Implications for bottom water formation: MODEL OF CIRCULATION BENEATH ICE SHELF, *Geophysical Research Letters*, *29*(8), 34–1–34–4, doi:10.1029/2001GL014589.

Jenkins, A., K. W. Nicholls, and H. F. J. Corr (2010), Observation and Parameterization of Ablation at the Base of Ronne Ice Shelf, Antarctica, *Journal of Physical Oceanography*, *40*(10), 2298–2312, doi:10.1175/2010JPO4317.1.

Jourdain, N. C., P. Mathiot, N. Merino, G. Durand, J. Le Sommer, P. Spence, P. Dutrieux, and G. Madec (2017), Ocean circulation and sea-ice thinning induced by melting ice shelves in the Amundsen Sea, *Journal of Geophysical Research: Oceans*, doi:10.1002/2016JC012509.

Jourdain, N. C., J.-M. Molines, J. L. Sommer, P. Mathiot, J. Chanut, C. de Lavergne, and G. Madec (2019), Simulating or prescribing the influence of tides on the Amundsen Sea ice shelves, *Ocean Modelling*, *133*, 44–55, doi:10.1016/j.ocemod.2018.11.001.

Jullion, L., A. C. N. Garabato, S. Bacon, M. P. Meredith, P. J. Brown, S. Torres-Valdés, K. G. Speer, P. R. Holland, J. Dong, D. Bakker, M. Hoppema, B. Loose, H. J. Venables, W. J. Jenkins, M.-J. Messias, and E. Fahrbach (2014), The contribution of the Weddell Gyre to the lower limb of the Global Overturning Circulation, *Journal of Geophysical Research: Oceans*, *119*(6), 3357–3377, doi:10.1002/2013JC009725.

King, M. A., L. Padman, K. Nicholls, P. J. Clarke, G. H. Gudmundsson, B. Kulessa, A. Shepherd, and Gourmelen, Noel (2011), Ocean tides in the Weddell Sea: New observations on the Filchner-Ronne and Larsen C ice shelves and model validation, *Journal of Geophysical Research*, *116*(C6), doi:10.1029/2011JC006949.

Klatt, O., E. Fahrbach, M. Hoppema, and G. Rohardt (2005), The transport of the Weddell Gyre across the Prime Meridian, *Deep Sea Research Part II: Topical Studies in Oceanography*, *52*(3-4), 513–528, doi:10.1016/j.dsr2.2004.12.015.

Large, W. G., and S. G. Yeager (2009), The global climatology of an interannually varying air–sea flux data set, *Climate Dynamics*, *33*(2-3), 341–364, doi:10.1007/s00382-008-0441-3.

Lewis, E. L., and R. G. Perkin (1986), Ice pumps and their rates, *Journal of Geophysical Research*, *91*(C10), 11,756, doi:10.1029/JC091iC10p11756.

Losch, M. (2008), Modeling ice shelf cavities in a *z* coordinate ocean general circulation model, *Journal of Geophysical Research*, *113*(C8), doi:10.1029/2007JC004368.

Lyard, F., F. Lefevre, T. Letellier, and O. Francis (2006), Modelling the global ocean tides: modern insights from fes2004, *Ocean Dyn.*, *56*(5–6), 394–415.

Mackensen, A. (2001), Oxygen and carbon stable isotope tracers of Weddell Sea water masses: new data and some paleoceanographic implications, *Deep-Sea Research I*, *48*, 1401–1422.

Madec, G., and NEMO-team (2016), Nemo ocean engine, version 3.6 stable, note du ple de mod lisation de l'institut pierre-simon laplace no. 27, *Technical Report. IPSL, France*.

Makinson, K., and K. W. Nicholls (1999), Modeling tidal currents beneath Filchner-Ronne Ice Shelf and on the adjacent continental shelf: Their effect on mixing and transport, *Journal of Geophysical Research: Oceans*, *104*(C6), 13,449–13,465, doi:10.1029/1999JC900008.

Makinson, K., M. Schröder, and S. Østerhus (2006), Effect of critical latitude and seasonal stratification on tidal current profiles along Ronne Ice Front, Antarctica, *Journal of Geophysical Research*, *111*(C3), doi:10.1029/2005JC003062.

Makinson, K., P. R. Holland, A. Jenkins, K. W. Nicholls, and D. M. Holland (2011), Influence of tides on melting and freezing beneath Filchner-Ronne Ice Shelf, Antarctica: SUB-ICE SHELF MELTING AND FREEZING, *Geophysical Research Letters*, *38*(L06601), doi:10.1029/2010GL046462.

Marsh, R., V. O. Ivchenko, N. Skliris, S. Alderson, G. R. Bigg, G. Madec, A. T. Blaker, Y. Aksenov, B. Sinha, A. C. Coward, J. Le Sommer, N. Merino, and V. B. Zalesny (2015), NEMO–ICB (v1.0): Interactive icebergs in the NEMO ocean model globally configured at eddy-permitting resolution, *Geoscientific Model Development*, *8*(5), 1547–1562, doi:10.5194/gmd-8-1547-2015.

Mathiot, P., A. Jenkins, C. Harris, and G. Madec (2017), Explicit and parametrised representation of under ice shelf seas in a z* coordinate ocean model, *Geoscientific Model Development Discussions*, pp. 1–43, doi:10.5194/gmd-2017-37.

Merino, N., N. C. Jourdain, J. Le Sommer, H. Goosse, P. Mathiot, and G. Durand (2018), Impact of increasing antarctic glacial freshwater release on regional sea-ice cover in the Southern Ocean, *Ocean Modelling*, *121*, 76–89, doi:10.1016/j.ocemod.2017.11.009.

Moholdt, G., L. Padman, and H. A. Fricker (2014), Basal mass budget of Ross and Filchner-Ronne ice shelves, Antarctica, derived from Lagrangian analysis of ICESat altimetry:

Ice shelf basal melting from altimetry, *Journal of Geophysical Research: Earth Surface*, *119*(11), 2361–2380, doi:10.1002/2014JF003171.

Mueller, R. D., L. Padman, M. S. Dinniman, S. Y. Erofeeva, H. A. Fricker, and M. A. King (2012), Impact of tide-topography interactions on basal melting of Larsen C Ice Shelf, Antarctica: LARSEN C TIDES AND BASAL MELT, *Journal of Geophysical Research: Oceans*, *117*(C05005), doi:10.1029/2011JC007263.

Mueller, R. D., T. Hattermann, S. L. Howard, and L. Padman (2018), Tidal influences on a future evolution of the Filchner–Ronne Ice Shelf cavity in the Weddell Sea, Antarctica, *The Cryosphere*, *12*(2), 453–476, doi:10.5194/tc-12-453-2018.

Naughten, K. A., K. J. Meissner, B. K. Galton-Fenzi, M. H. England, R. Timmermann, and H. H. Hellmer (2018a), Future Projections of Antarctic Ice Shelf Melting Based on CMIP5 Scenarios, *Journal of Climate*, *31*(13), 5243–5261, doi:10.1175/JCLI-D-17-0854.1.

Naughten, K. A., K. J. Meissner, B. K. Galton-Fenzi, M. H. England, R. Timmermann, H. H. Hellmer, T. Hattermann, and J. B. Debernard (2018b), Intercomparison of Antarctic ice-shelf, ocean, and sea-ice interactions simulated by MetROMS-iceshelf and FESOM 1.4, *Geoscientific Model Development*, *11*(4), 1257–1292, doi:10.5194/gmd-11-1257-2018.

Naveira Garabato, A. C., J. D. Zika, L. Jullion, P. J. Brown, P. R. Holland, M. P. Meredith, and S. Bacon (2016), The thermodynamic balance of the Weddell Gyre: THERMODYNAMICS OF THE WEDDELL GYRE, *Geophysical Research Letters*, *43*(1), 317–325, doi:10.1002/2015GL066658.

Nicholls, K. W., and S. Østerhus (2004), Interannual variability and ventilation timescales in the ocean cavity beneath Filchner-Ronne Ice Shelf, Antarctica, *Journal of Geophysical Research*, *109*(C4), doi:10.1029/2003JC002149.

Nicholls, K. W., K. Makinson, and A. V. Robinson (1991), Ocean circulation beneath the Ronne ice shelf, *Nature*, *354*(6350), 221–223, doi:10.1038/354221a0.

Nicholls, K. W., K. Makinson, and M. R. Johnson (1997), New oceanographic data from beneath Ronne Ice Shelf, Antarctica, *Geophys. Res. Lett.*, *24*, 167–170.

Nicholls, K. W., S. Østerhus, K. Makinson, and M. R. Johnson (2001), Oceanographic conditions south of Berkner Island, beneath Filchner-Ronne Ice Shelf, Antarctica, *Journal of Geophysical Research: Oceans*, *106*(C6), 11,481–11,492, doi:10.1029/2000JC000350.

Nicholls, K. W., Makinson, Keith, and Østerhus, S. (2004), Circulation and water masses beneath the northern Ronne Ice Shelf, Antarctica, *Journal of Geophysical Research*, *109*(C12), doi:10.1029/2004JC002302.

Nicholls, K. W., S. Østerhus, K. Makinson, T. Gammelsrød, and E. Fahrbach (2009), Ice-ocean processes over the continental shelf of the southern Weddell Sea, Antarctica: A review, *Reviews of Geophysics*, *47*(3), doi:10.1029/2007RG000250.

Nowicki, S., and H. Seroussi (2018), Projections of Future Sea Level Contributions from the Greenland and Antarctic Ice Sheets: Challenges Beyond Dynamical Ice Sheet Modeling, *Oceanography*, *31*(2), doi:10.5670/oceanog.2018.216.

O'Reilly, J. E., S. Maritorena, B. G. Mitchell, D. A. Siegel, K. L. Carder, S. A. Garver, M. Kahru, and C. McClain (1998), Ocean color chlorophyll algorithms for SeaWiFS, *J. Geophys. Res.*, *103*(C11), 24,937–24,953.

Orsi, A., G. Johnson, and J. Bullister (1999), Circulation, mixing, and production of Antarctic Bottom Water, *Progress in Oceanography*, *43*(1), 55–109, doi:10.1016/S0079-6611(99)00004-X.

Orsi, A. H., W. D. Nowlin, and T. Whitworth (1993), On the circulation and stratification of the Weddell Gyre, *Deep Sea Research Part I: Oceanographic Research Papers*, *40*(1), 169–203, doi:10.1016/0967-0637(93)90060-G.

Orsi, A. H., T. Whitworth, and W. D. Nowlin (1995), On the meridional extent and fronts of the Antarctic Circumpolar Current, *Deep Sea Research Part I: Oceanographic Research Papers*, *42*(5), 641–673, doi:10.1016/0967-0637(95)00021-W.

Orsi, A. H., W. M. Smethie, and J. L. Bullister (2002), On the total input of Antarctic waters to the deep ocean: A preliminary estimate from chlorofluorocarbon measurements, *Journal of Geophysical Research*, *107*(C8), doi:10.1029/2001JC000976.

Padman, L., M. R. Siegfried, and H. A. Fricker (2018), Ocean Tide Influences on the Antarctic and Greenland Ice Sheets: Tide Influences on Ice Sheets, *Reviews of Geophysics*, *56*(1), 142–184, doi:10.1002/2016RG000546.

Pereira, A. F., A. Beckmann, and H. H. Hellmer (2002), Tidal Mixing in the Southern Weddell Sea: Results from a Three-Dimensional Model, *Journal of Physical Oceanography*, *32*(7), 2151–2170, doi:10.1175/1520-0485(2002)032⟨2151:TMITSW⟩2.0.CO;2.

Purkey, S. G., W. M. Smethie, G. Gebbie, A. L. Gordon, R. E. Sonnerup, M. J. Warner, and J. L. Bullister (2018), A Synoptic View of the Ventilation and Circulation of Antarctic Bottom Water from Chlorofluorocarbons and Natural Tracers, *Annual Review of Marine Science*, *10*(1), 503–527, doi:10.1146/annurev-marine-121916-063414.

Reese, R., G. H. Gudmundsson, A. Levermann, and R. Winkelmann (2018), The far reach of ice-shelf thinning in Antarctica, *Nature Climate Change*, *8*(1), 53–57, doi:10.1038/s41558-017-0020-x.

Reeve, K. A., O. Boebel, V. Strass, T. Kanzow, and R. Gerdes (2019), Horizontal circulation and volume transports in the Weddell Gyre derived from Argo float data, *Progress in Oceanography*, *175*, 263–283, doi:10.1016/j.pocean.2019.04.006.

Rignot, E., S. Jacobs, J. Mouginot, and B. Scheuchl (2013), Ice-Shelf Melting Around Antarctica, *Science*, *341*(6143), 266–270, doi:10.1126/science.1235798.

Rignot, E., J. Mouginot, B. Scheuchl, M. van den Broeke, M. J. van Wessem, and M. Morlighem (2019), Four decades of Antarctic Ice Sheet mass balance from 1979–2017, *Proceedings of the National Academy of Sciences*, *116*(4), 1095–1103, doi:10.1073/pnas.1812883116.

Robertson, R. (2001a), Internal tides and baroclinicity in the Southern Weddell Sea: 2. Effects of

the critical latitude and stratification, *Journal of Geophysical Research: Oceans*, *106*(C11), 27,017–27,034, doi:10.1029/2000JC000476.

Robertson, R. (2001b), Internal tides and baroclinicity in the southern Weddell Sea: 1. Model description, *Journal of Geophysical Research: Oceans*, *106*(C11), 27,001–27,016, doi:10.1029/2000JC000475.

Robertson, R., L. Padman, and G. D. Egbert (1998), Tides in the Weddell Sea, in *Antarctic Research Series*, vol. 75, edited by S. S. Jacobs and R. F. Weiss, pp. 341–369, American Geophysical Union, Washington, D. C., doi:10.1029/AR075p0341.

Robinson, A., K. Makinson, and K. W. Nicholls (1994), The oceanic environment beneath the north-west Ronne Ice Shelf, Antarctica, *Ann. Glac.*, *20*, 386–390.

Roquet, F., G. Madec, T. McDougall, and P. Barker (2015), Accurate polynomial expressions for the density and specific volume of seawater using the TEOS-10 standard, *Ocean Modelling*, *90*, 29–43, doi:10.1016/j.ocemod.2015.04.002.

Rosier, S. H. R., C. Hofstede, A. M. Brisbourne, T. Hattermann, K. W. Nicholls, P. E. D. Davis, P. G. D. Anker, C.-D. Hillenbrand, A. M. Smith, and H. F. J. Corr (2018), A New Bathymetry for the Southeastern Filchner-Ronne Ice Shelf: Implications for Modern Oceanographic Processes and Glacial History, *Journal of Geophysical Research: Oceans*, doi:10.1029/2018JC013982.

Rousset, C., M. Vancoppenolle, G. Madec, T. Fichefet, S. Flavoni, A. Barthélemy, R. Benshila, J. Chanut, C. Levy, S. Masson, and F. Vivier (2015), The Louvain-La-Neuve sea ice model LIM3.6: Global and regional capabilities, *Geoscientific Model Development*, *8*(10), 2991–3005, doi:10.5194/gmd-8-2991-2015.

Ryan, S., T. Hattermann, E. Darelius, and M. Schröder (2017), Seasonal cycle of hydrography on the eastern shelf of the Filchner Trough, Weddell Sea, Antarctica: SEASONAL HYDROGRAPHY FILCHNER, *Journal of Geophysical Research: Oceans*, *122*(8), 6437–6453, doi:10.1002/2017JC012916.

Schodlok, M. P., D. Menemenlis, and E. J. Rignot (2016), Ice shelf basal melt rates around Antarctica from simulations and observations: ICE SHELF BASAL MELT AROUND ANTARCTICA, *Journal of Geophysical Research: Oceans*, *121*(2), 1085–1109, doi:10.1002/2015JC011117.

Schröder, L., M. Horwath, R. Dietrich, V. Helm, M. R. van den Broeke, and S. R. M. Ligtenberg (2019), Four decades of Antarctic surface elevation changes from multi-mission satellite altimetry, *The Cryosphere*, *13*(2), 427–449, doi:10.5194/tc-13-427-2019.

Schröder, M., and E. Fahrbach (1999), On the structure and the transport of the eastern weddell gyre, *Deep-Sea Research II*, *46*, 501–527.

Schureman, P. (1958), Manual of harmonic analysis and prediction of tides, *US Government Printing Office No. 98*.

Semper, S., and E. Darelius (2017), Seasonal resonance of diurnal coastal trapped waves in the southern Weddell Sea, Antarctica, *Ocean Science*, *13*(1), 77–93, doi:10.5194/os-13-77-2017.

Shepherd, A., H. A. Fricker, and S. L. Farrell (2018), Trends and connections across the Antarctic cryosphere, *Nature*, *558*(7709), 223–232, doi:10.1038/s41586-018-0171-6.

Smedsrud, L. H., and A. Jenkins (2004), Frazil ice formation in an ice shelf water plume, *Journal of Geophysical Research: Oceans*, *109*(C3), doi:10.1029/2003JC001851.

Stammer, D., R. D. Ray, O. B. Andersen, B. K. Arbic, W. Bosch, L. Carrère, Y. Cheng, D. S. Chinn, B. D. Dushaw, G. D. Egbert, S. Y. Erofeeva, H. S. Fok, J. A. M. Green, S. Griffiths, M. A. King, V. Lapin, F. G. Lemoine, S. B. Luthcke, F. Lyard, J. Morison, M. Müller, L. Padman, J. G. Richman, J. F. Shriver, C. K. Shum, E. Taguchi, and Y. Yi (2014), Accuracy assessment of global barotropic ocean tide models, *Reviews of Geophysics*, *52*(3), 243–282, doi:10.1002/2014RG000450.

Stewart, A. L., and A. F. Thompson (2015), Eddy-mediated transport of warm Circumpolar Deep Water across the Antarctic Shelf Break, *Geophysical Research Letters*, *42*(2), 432–440, doi:10.1002/2014GL062281.

Stewart, A. L., A. Klocker, and D. Menemenlis (2018), Circum-Antarctic Shoreward Heat Transport Derived From an Eddy- and Tide-Resolving Simulation, *Geophysical Research Letters*, *45*(2), 834–845, doi:10.1002/2017GL075677.

Storkey, D., A. T. Blaker, P. Mathiot, A. Megann, Y. Aksenov, E. W. Blockley, D. Calvert, T. Graham, H. T. Hewitt, P. Hyder, T. Kuhlbrodt, J. G. L. Rae, and B. Sinha (2018), UK Global Ocean GO6 and GO7: A traceable hierarchy of model resolutions, *Geoscientific Model Development*, *11*(8), 3187–3213, doi:10.5194/gmd-11-3187-2018.

The IMBIE team (2018), Mass balance of the Antarctic Ice Sheet from 1992 to 2017, *Nature*, *558*(7709), 219–222, doi:10.1038/s41586-018-0179-y.

Thompson, A. F., and K. J. Heywood (2008), Frontal structure and transport in the northwestern Weddell Sea, *Deep Sea Research Part I: Oceanographic Research Papers*, *55*(10), 1229–1251, doi:10.1016/j.dsr.2008.06.001.

Thompson, A. F., A. L. Stewart, P. Spence, and K. J. Heywood (2018), The Antarctic Slope Current in a Changing Climate, *Reviews of Geophysics*, *56*(4), 741–770, doi:10.1029/2018RG000624.

Timmermann, R., and S. Goeller (2017), Response to Filchner–Ronne Ice Shelf cavity warming in a coupled ocean–ice sheet model – Part 1: The ocean perspective, *Ocean Science*, *13*(5), 765–776, doi:10.5194/os-13-765-2017.

Timmermann, R., and H. H. Hellmer (2013), Southern Ocean warming and increased ice shelf basal melting in the twenty-first and twenty-second centuries based on coupled ice-ocean finite-element modelling, *Ocean Dynamics*, *63*(9-10), 1011–1026, doi:10.1007/s10236-013-0642-0.

Timmermann, R., A. Beckmann, and H. H. Hellmer (2002), Simulations of ice-ocean dynamics in the Weddell Sea 1. Model configuration and validation, *Journal of Geophysical Research*, *107*(C3), doi:10.1029/2000JC000741.

Timmermann, R., Q. Wang, and H. Hellmer (2012), Ice-shelf basal melting in a global finite-element sea-ice/ice-shelf/ocean model, *Annals of Glaciology*, *53*(60), 303–314, doi:10.3189/2012AoG60A156.

Vancoppenolle, M., T. Fichefet, H. Goosse, S. Bouillon, G. Madec, and M. A. M. Maqueda (2009), Simulating the mass balance and salinity of Arctic and Antarctic sea ice. 1. Model description and validation, *Ocean Modelling*, *27*(1-2), 33–53, doi:10.1016/j.ocemod.2008.10.005.

# List of Tables



# Figure Captions

1 **Regional model configuration** in its geographical context (pink dashes: computational domain, pink solid lines: locations of model open boundaries, outside of which ocean regions are masked in the configuration, but not in the present figure). Ice fronts are contoured in dark gray. Colors show model ocean water column depth $h_{water}$, which, in ice-shelf cavities, is given by the difference between model bathymetry (light gray contours) and ice draft. Figure axes are parallel to the model grid, longitude and latitudes are dotted, and model isotropic horizontal resolution (km) contoured in purple. For context, observed climatological March & September sea-ice edges are also contoured (white dotted & dashed). Place names indicated are Joinville Island (JI), South Shetland Islands (sSI), Bransfield Strait (BS), South Orkney islands (sOI); Fimbul (Fi), Jelbart (Je), Atka (At), Ekstroem (Ek), Quar (Q), Riiser-Larsen (Ri-L), Brunt/Stancomb-Wills (B/St-W), and Larsen G, F, E, D, C ice shelves, as well as the the SCAR inlet & Seal Nunatak glaciers (remnants of Larsen A & B: rB & rA). Furthermore within the Filchner-Ronne ice-shelf (FRIS) cavity: Berkner Island (BI), South Channel (SCh), Korff & Henry ice rises (Kir & Hir) and Doake rumples (Dr). FRIS sub-ice-shelf mooring locations are indicated by '+'s. . . . . 60

**Table 1 | Southwestern Weddell Sea ice-shelf melt: integral statistics, and role of tides.**[a]

| | | EWIS | FRIS | LARSEN | Weddell |
|---|---|---|---|---|---|
| $\mathcal{M}_{tide}$ | net | -55.1 ±*35.6* | -159.2 ±*27.8* | -42.9 ±*29.7* | -257.2 ±*63.0*[b] |
| | melt | -58.8 ±*35.4* | -247.9 ±*34.8* | -43.8 ±*29.5* | -350.5 ±*67.5* |
| | freeze | 3.6 ± *0.6* | 88.7 ± *9.9* | 0.9 ± *0.2* | 93.3 ± *9.9* |
| $\mathcal{M}_{notide}$ | net | -36.2 ±*24.5* | -105.2 ±*15.1* | -24.0 ±*12.5* | -165.4 ±*32.3* |
| | melt | -36.9 ±*24.4* | -136.4 ±*17.0* | -24.5 ±*12.4* | -197.8 ±*33.4* |
| | freeze | 0.7 ± *0.2* | 31.2 ± *4.6* | 0.5 ± *0.2* | 32.4 ± *4.7* |
| $\Delta\mathcal{M}$ | net | -18.9 ±*13.5* | -54.0 ±*17.0* | -18.9 ±*18.3* | -91.8 ±*38.6* |
| | melt | -21.9 ±*13.5* | -111.5 ±*21.0* | -19.3 ±*18.3* | 152.6 ±*41.3* |
| | freeze | 3.0 ± *0.5* | 57.5 ± *7.0* | 0.4 ± *0.1* | 60.8 ± *7.1* |

Notes: [a] Year 4-8 (1993-1997) 5-year averages of integral ice-shelf melt $\mathcal{M}$ ($< 0$ for melting), $\pm$ one standard deviation of 45-day running means around the 5-year average, all in $Gt/yr$: in the reference experiment with tides, in the perturbation experiment without tides, and their difference $\Delta \equiv$ tide $-$ notide. For each, the first row gives the net integral, and the following two the integral obtained separately for regions of basal melting and basal freezing. [b] In comparison, the net calving iceberg melt freshwater flux integrated over the domain amounts to -274.8 $\pm$ 219.7 $Gt/yr$.

**Table 2 | Mechanisms of the tidal impact on Weddell Sea ice-shelf melting.**[a]

| | EWIS | FRIS | LARSEN | Weddell |
|---|---|---|---|---|
| $\Delta\mathcal{M}$ | -18.9 ±*13.5* | -54.0 ±*17.0* | -18.9 ±*18.3* | -91.8 ± *38.6* |
| $\Delta\mathcal{M}_{DYN}$ | -132.8 ±*37.0* | -494.1 ±*54.3* | -132.8 ±*56.8* | -759.6 ±*111.0* |
| $\Delta\mathcal{M}_{THERM}$ | 17.0 ± *8.6* | 76.9 ± *9.5* | 17.0 ± *7.0* | 110.9 ± *16.6* |
| $\Delta\mathcal{M}_{COV}$ | 96.3 ±*19.8* | 362.9 ±*40.4* | 96.4 ±*33.0* | 555.6 ± *69.7* |
| *residual* | *0.6* ± *0.1* | *0.3* ± *0.2* | *0.5* ± *0.2* | *1.4* ± *0.2* |

Notes: [a] The net tidal signature ($\Delta \equiv tide - notide$) in integral ice-shelf melt $\mathcal{M}$ ($< 0$ melt) (row repeated from Table 1), and its dynamical $\Delta\mathcal{M}_{DYN}$, thermodynamical $\Delta\mathcal{M}_{THERM}$ and covariational $\Delta\mathcal{M}_{COV}$ contributions, as given by (2), as well as a $residual$ (net minus sum of contributions). Otherwise as in Table 1, i.e. based on year 4–8 5-year averages (1993–1997), and in $Gt/yr$.

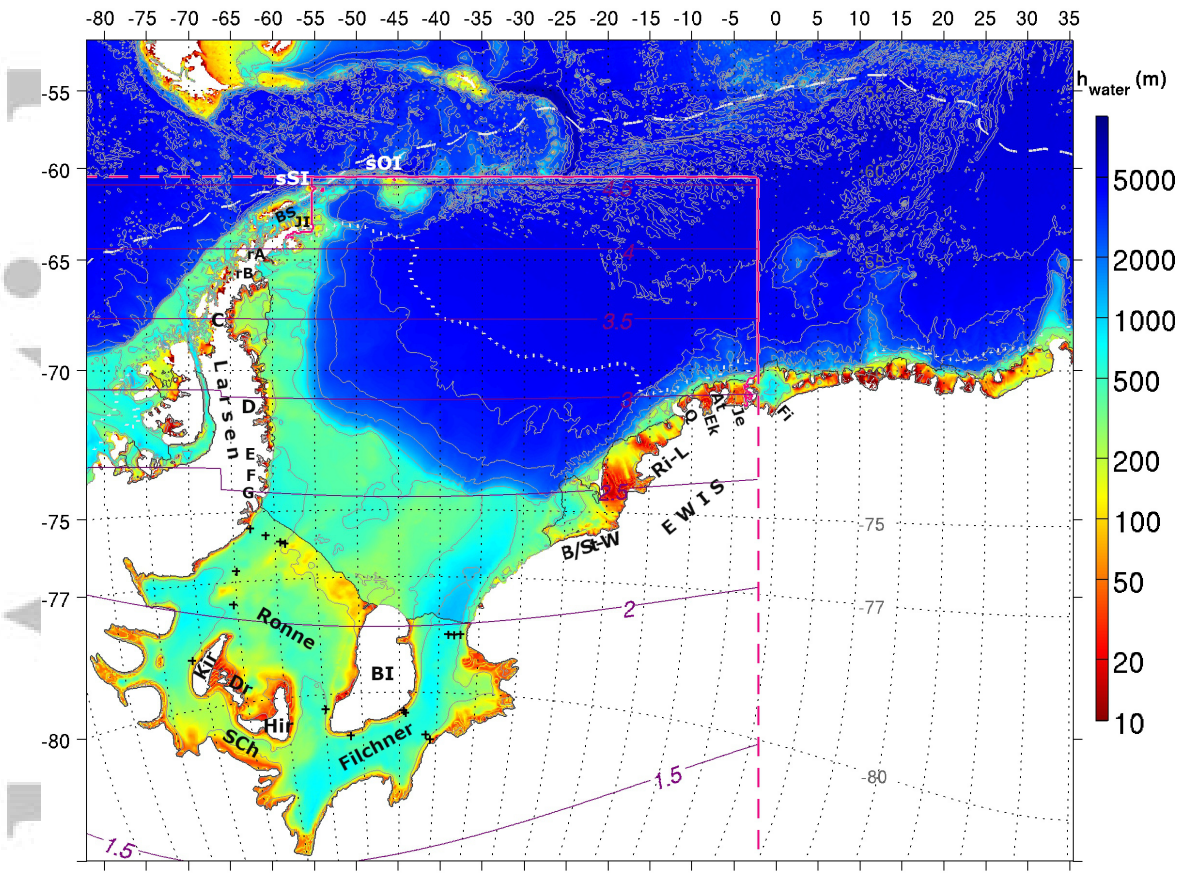


**Figure 1 | Regional model configuration** in its geographical context (pink dashes: computational domain, pink solid lines: locations of model open boundaries, outside of which ocean regions are masked in the configuration, but not in the present figure). Ice fronts are contoured in dark gray. Colors show model ocean water column depth $h_{water}$, which, in ice-shelf cavities, is given by the difference between model bathymetry (light gray contours) and ice draft. Figure axes are parallel to the model grid, longitude and latitudes are dotted, and model isotropic horizontal resolution (km) contoured in purple. For context, observed climatological March & September sea-ice edges are also contoured (white dotted & dashed). Place names indicated are Joinville Island (JI), South Shetland Islands (sSI), Bransfield Strait (BS), South Orkney islands (sOI); Fimbul (Fi), Jelbart (Je), Atka (At), Ekstroem (Ek), Quar (Q), Riiser-Larsen (Ri-L), Brunt/Stancomb-Wills (B/St-W), and Larsen G, F, E, D, C ice shelves, as well as the the SCAR inlet & Seal Nunatak glaciers (remnants of Larsen A & B: rB & rA). Furthermore within the Filchner-Ronne ice-shelf (FRIS) cavity: Berkner Island (BI), South Channel (SCh), Korff & Henry ice rises (Kir & Hir) and Doake rumples (Dr). FRIS sub-ice-shelf mooring locations are indicated by '+'s.

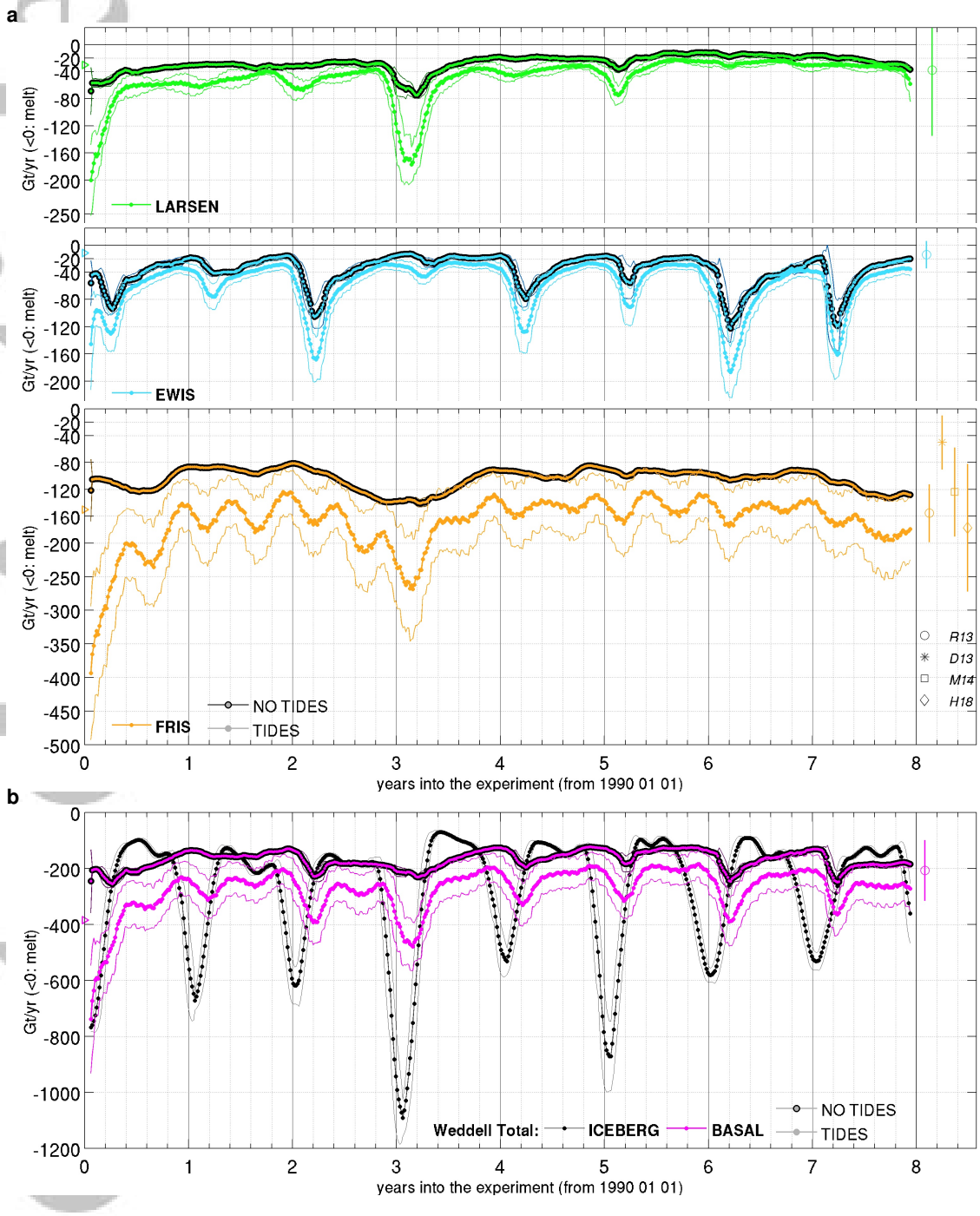


**Figure 2 | Weddell Sea integral ice-shelf melt timeseries** $\mathcal{M}(t)$ ($<0$ melt). **a** Integrated by ice-shelf formation (colored as labelled): in the reference experiment with tides (color spheres give 45-day running means & lines their one-standard-deviation envelopes of 5-day-average timeseries), contrasted to the experiment without tides (black-edge color spheres & darker colored standard-deviation lines, here often coinciding with symbol size). Symbols on the rhs show corresponding available long-term mean observational estimates, by *Rignot et al.* (2013, R13, ○), *Depoorter et al.* (2013, D13, ∗), *Moholdt et al.* (2014, M14, □) and *Huhn et al.* (2018, H18, ◇). Triangles at the timeaxis origin give the constant prescribed melt of the forcing simulation. **b** As **a**, but for the Weddell domain total, and in comparison to the interannually-varying melt of drifting icebergs

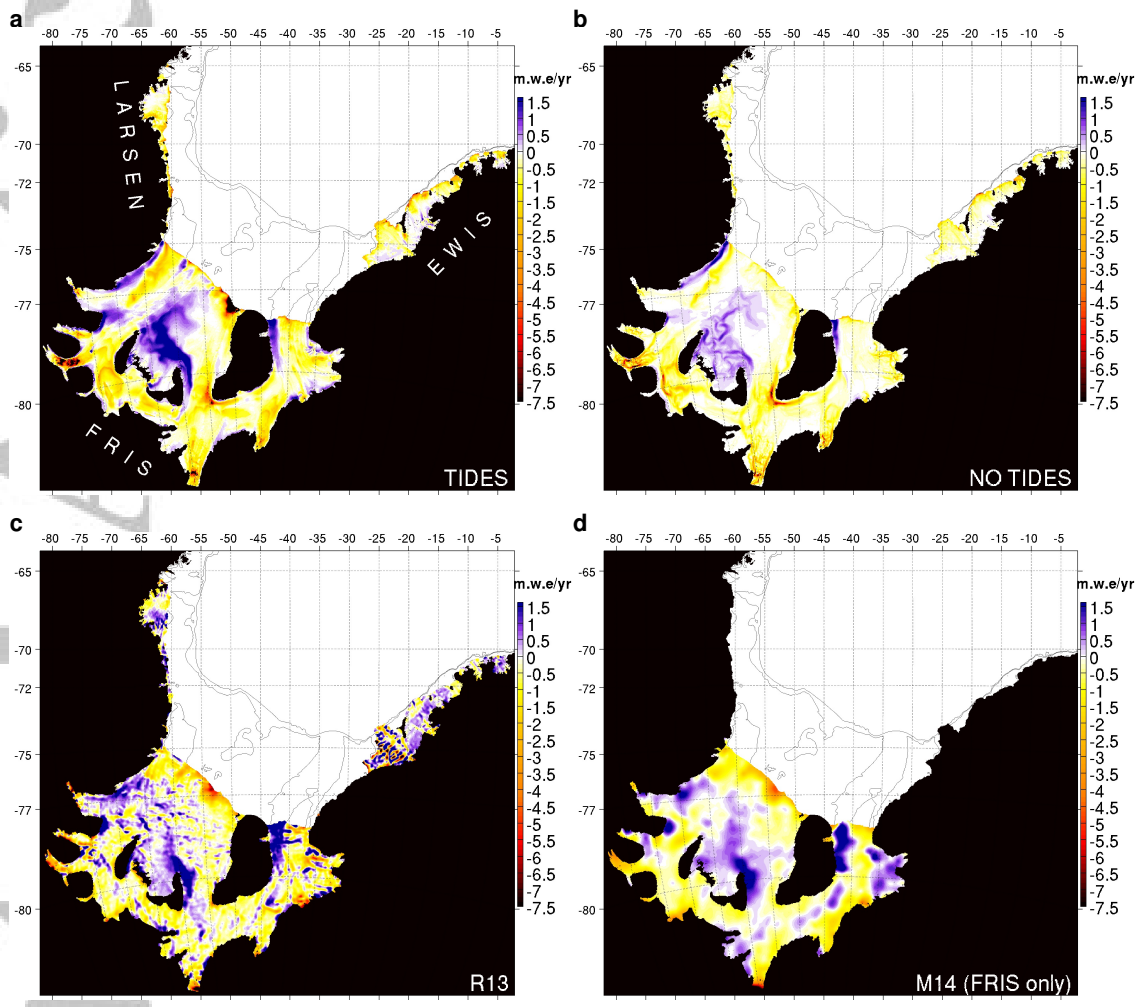


**Figure 3 | Ice-shelf basal melt maps.** Maps of the last 5-year (1993-1997) average basal melt $\mathcal{M}$ ($<$0 melt) in the reference experiment with tides **(a)**, contrasted to the perturbation experiment without tides **(b)**. For comparison, available long-term mean observational estimates by *Rignot et al.* (2013, R13) & *Moholdt et al.* (2014, M14) are shown in **(c)** & **(d)**, the latter available for FRIS only.

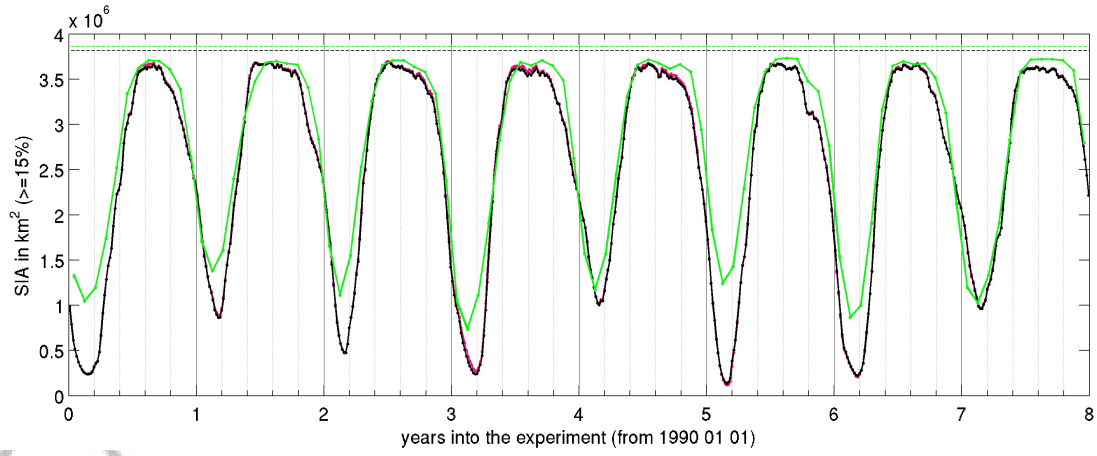


**Figure 4 | Sea-ice concentration.** Timeseries of sea-ice area in the regional configuration reference experiment (as 5-day averages, black; corresponding no-tide perturbation experiment sea-ice area timeseries, shown in purple, differ little), in comparison to monthly-mean microwave observations (green, bootstrap version 2), both integrated over the Weddell ocean model domain. (The sea-ice area metric shown here integrates the fractional sea-ice covered area of grid points for which area concentration exceeds a 15 % threshold. For reference, dashed lines indicate the domain's total ocean area in the two grids).

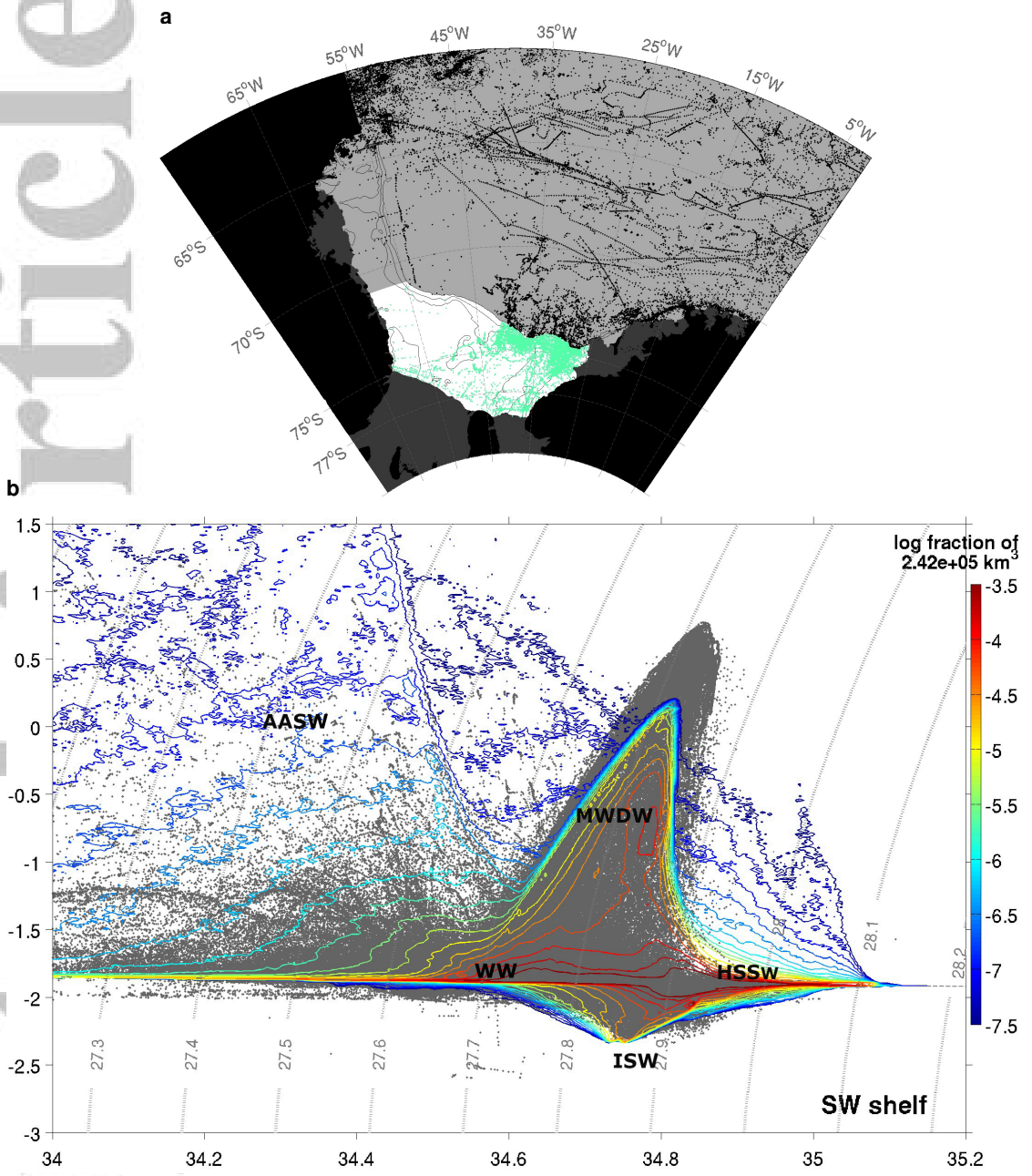


**Figure 5 | Open-ocean water masses.** Reference experiment 5-year average (years 4-8, i.e. 1993-1997) volumetric $\Theta$-$S_A$ for the south-western Weddell continental shelf (light-shaded region in **a**) displayed by colored contours in **b** (as log fraction of the region's total ocean volume; gray dotted contours indicate $\sigma_0$). All-time available in-situ observations collected in the region (locations mapped by green dots in **a**) are superimposed on the regional $\Theta$-$S_A$ diagram in **b** by gray dots. Major water-mass types are: modified warm deep water (MWDW), winter water (WW), high-salinity shelf water (HSSW), ice-shelf water (ISW) and Antarctic surface water (AASW). (See Supplement for corresponding simulated water-mass diagrams in the other open-ocean regions and their comparison to the in-situ observations collected there, at the locations mapped by black dots in **a**).

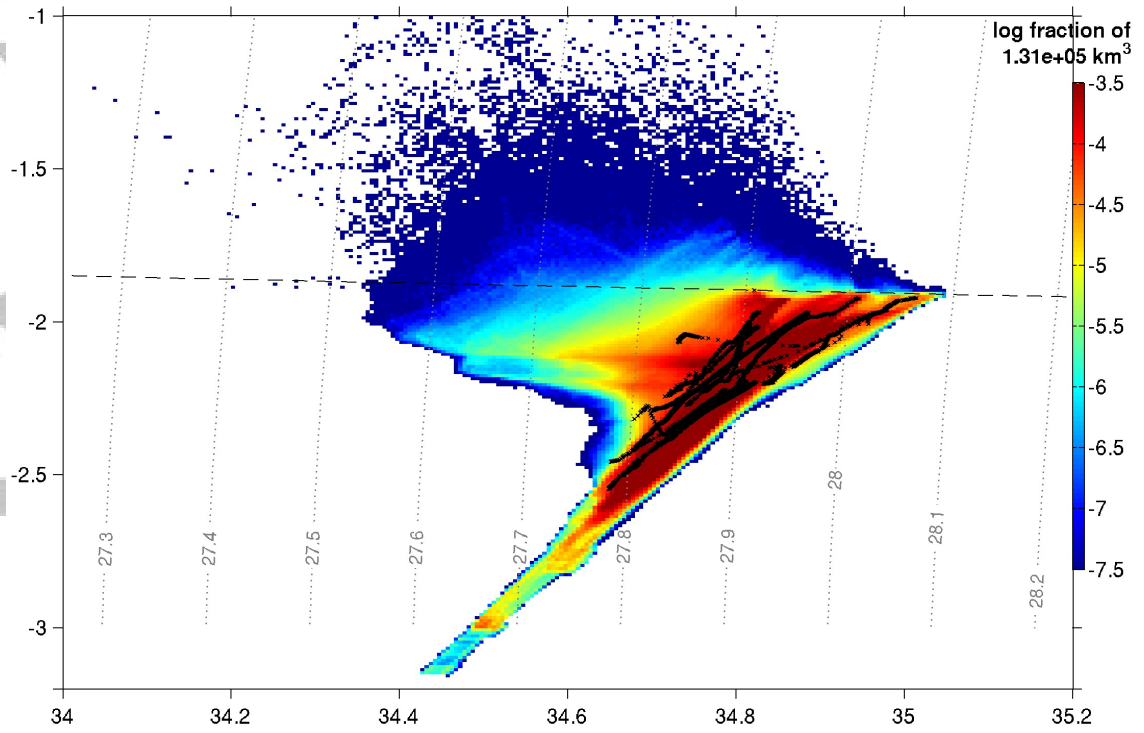


**Figure 6 | FRIS cavity water masses.** Reference experiment 5-year average (years 4-8, i.e. 1993–1997) volumetric $\Theta$-$S_A$ for the FRIS cavity, shown as log fraction of the cavity's total ocean volume (color shading). FRIS sub-ice-shelf CTD data from mooring boreholes (mapped in Fig. 1, see text for details) are superimposed for comparison (black crosses). (See Supplement for corresponding water-mass diagrams of EWIS and Larsen ice-shelf cavities.)

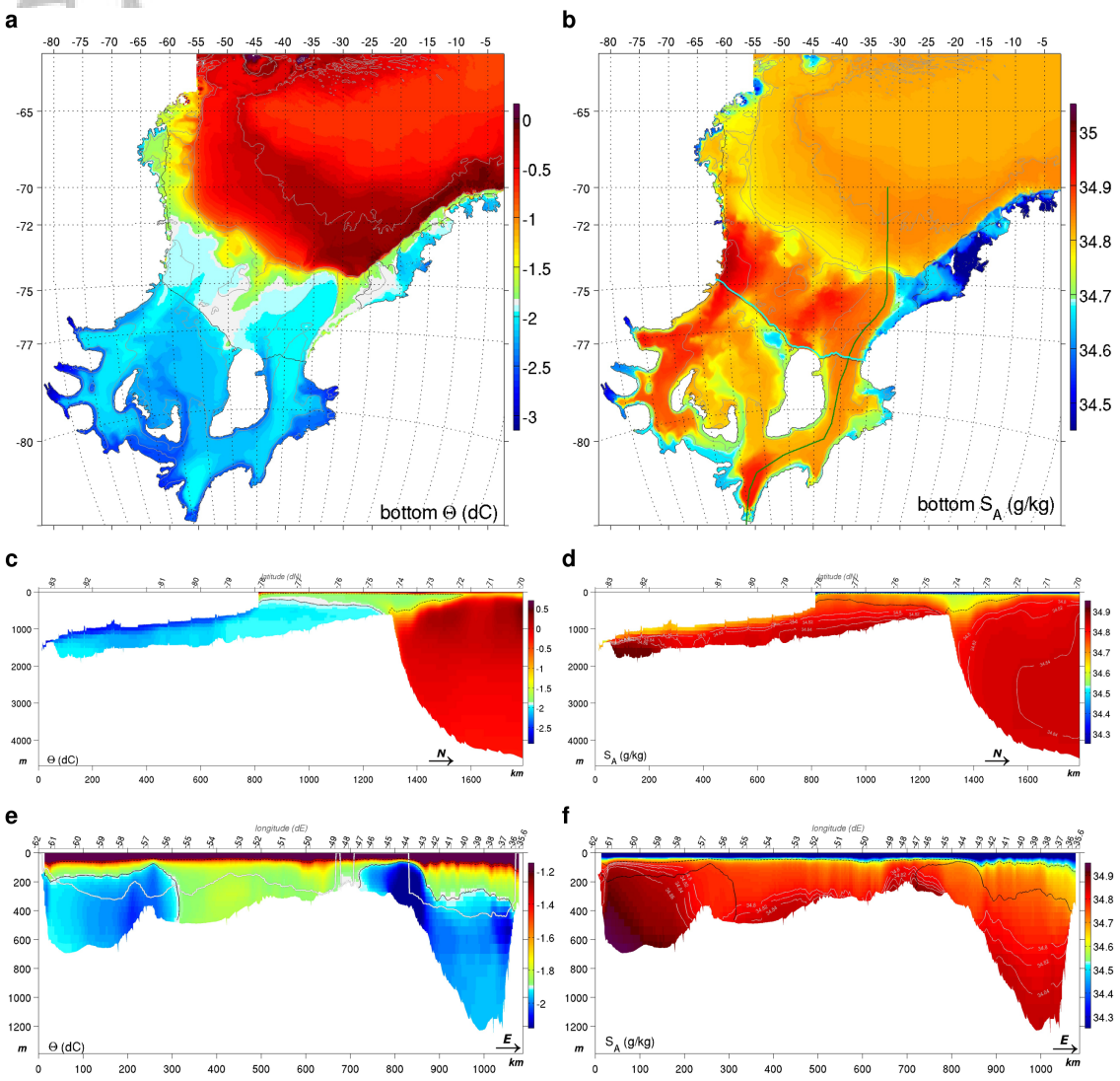


**Figure 7 | Illustration of the water mass structure in the reference experiment.** 5-year average February (years 4-8, i.e. 1993-1997) conservative temperature Θ & absolute salinity $S_A$: **a** & **b** at the sea floor, **c** & **d** along a vertical section crossing from the open gyre in the north, across Filchner sill & Trough through the Filchner cavity towards the Foundation ice stream grounding line (along the green line in **b**), and **e** & **f** along a vertical section across the southwestern Weddell Sea continental shelf just north of the FRIS ice front (along the cyan line in **b**, which near-coincides with the ice front contoured in dark gray just to its south). Contours in **a,b** show bathymetry (light gray) and ice fronts (dark gray), in **c–f** Θ isotherms of -1.9 & -1.4 °C (solid & dashed black, the latter often barely visible as close to the surface), and additionally highlight in **d,f** selected $S_A$ contours (gray), and in **e** the depth of the ice draft just to the south (white-gray).

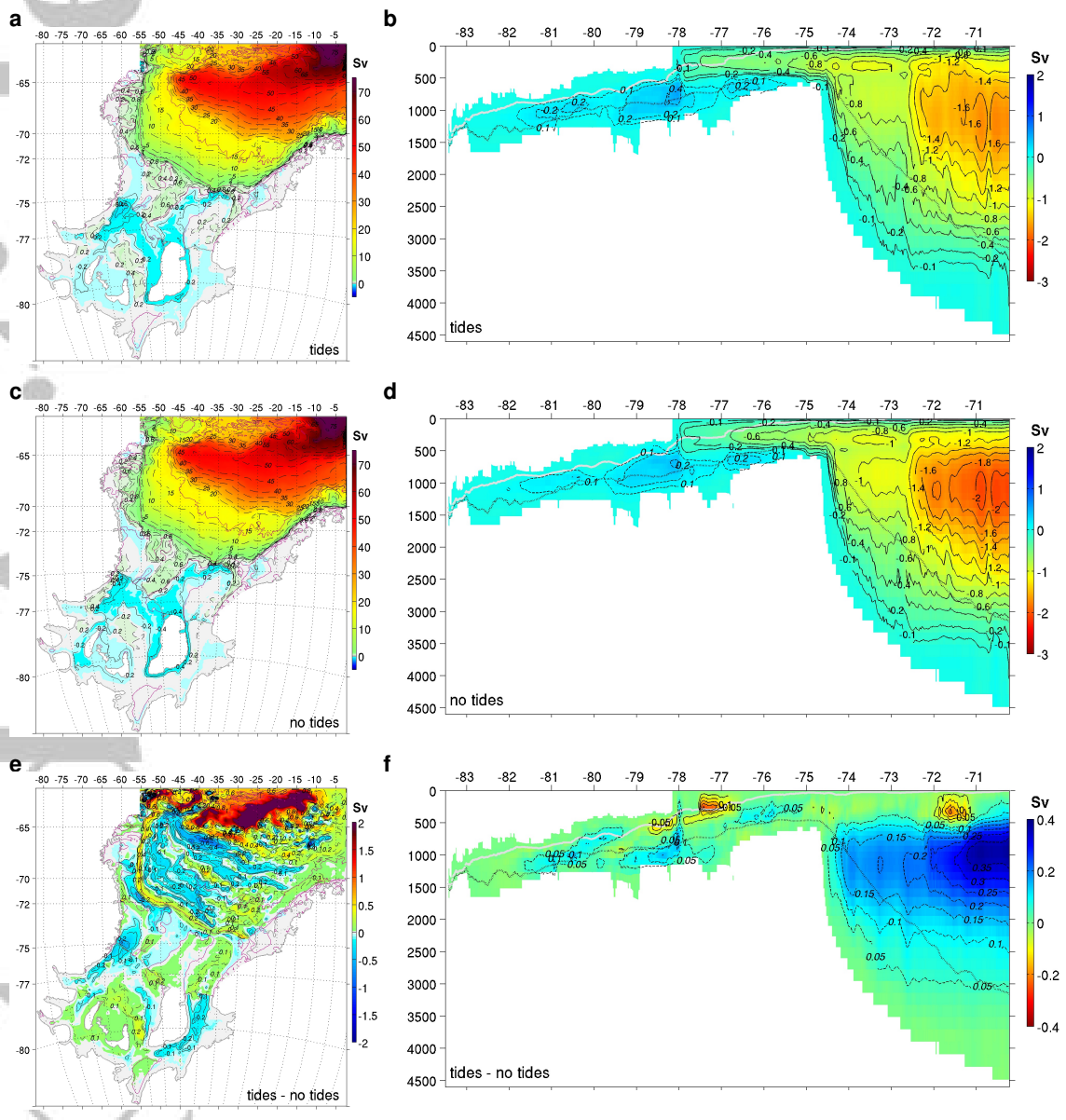


**Figure 8 | Integral metrics of circulation.** **a,c,e** Barotropic, and **b,d,f** meridional overturning streamfunctions, for the years 4-8 average (1993-1997), both colored and contoured in Sv (dashed contours denote positive streamfunction values, and note the reversed color scale in b,d,f vs a,c,e): **a,b** in presence of tides, and **c,d** in absence of tides; **e,f** display the tidal signal itself ($\Delta \equiv$ tides $-$ no tides). Additional contours are in **a,c,e** 400, 1500 & 4000m isobaths (purple), icefronts (gray), as well as latitude, longitude (dotted), and in **b,d,f** the weighted-average ice draft & sea floor depths (gray line & black dots).

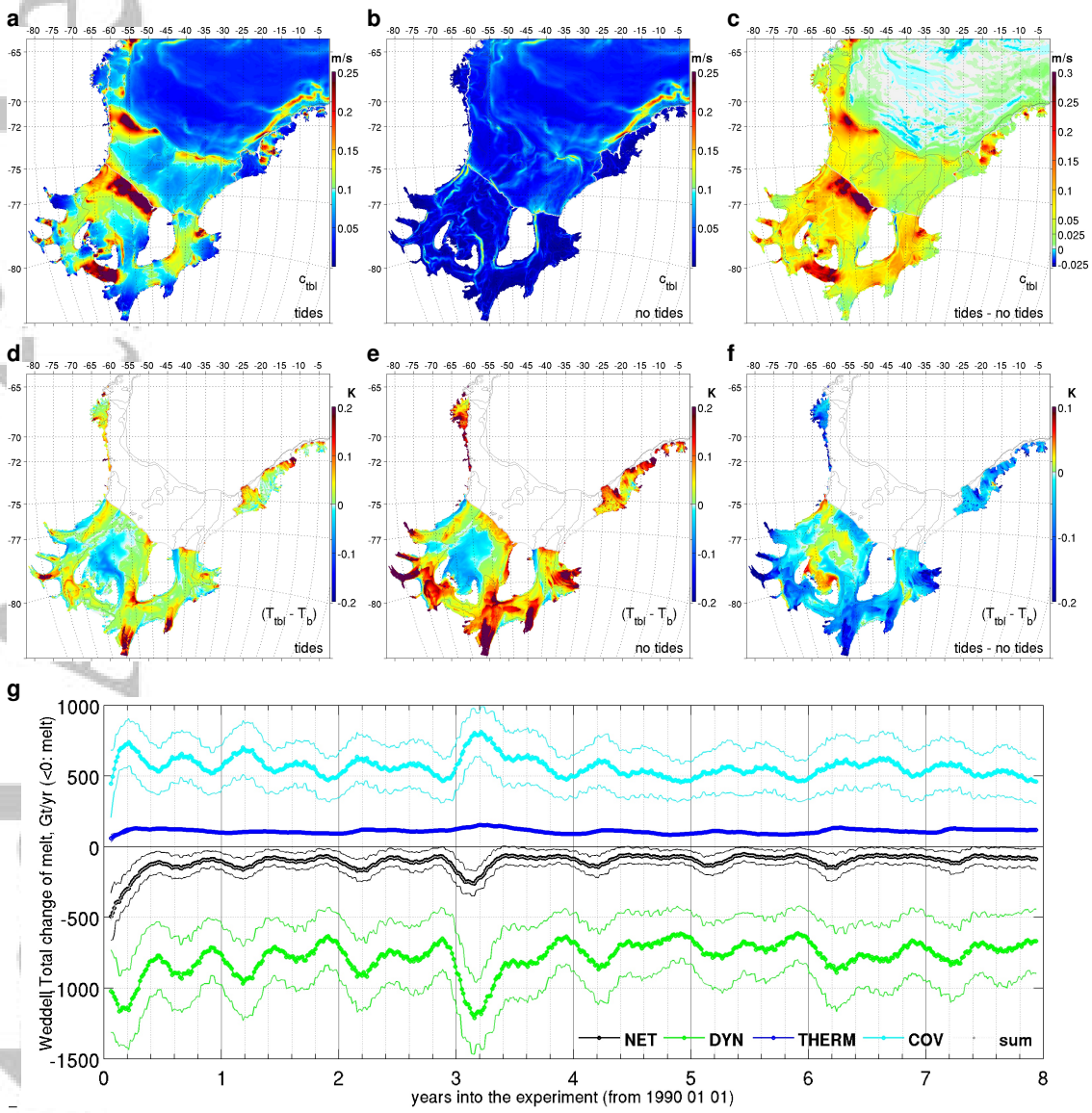


**Figure 9 | Mechanisms of the tidal impact on Weddell Sea ice-shelf melting.** Top panels **(a,b,c)** map the sub-ice-shelf ocean boundary layer flow speed $c_{tbl}$ (in m/s; in the open ocean top 30 m speed is mapped for reference), panels below **(d,e,f)** the departure of the sub-ice-shelf boundary layer ocean temperature from the freezing point at the ice base (in K): on the lhs **(a,d)** in presence of tides, in the middle **(b,e)** without tides, and on the rhs **(c,f)** the tidal signature $\Delta$. All maps show year 4–8 averages, and contour 500 & 1000 m isobaths for reference. Panel **g** displays timeseries of the tide-driven Weddell ice-shelf melt $\Delta\mathcal{M}(t)$ (black, <0 melt), and reconstructs these, following Eq. (2), from dynamical (green), thermodynamical (blue) and covariational (cyan) mechanistic contributions, with the sum of the three latter (gray dots) visibly coincident with the net change. (As in Fig. 2, 45-day running means of 5-day averages and their one standard deviation envelopes are shown.)

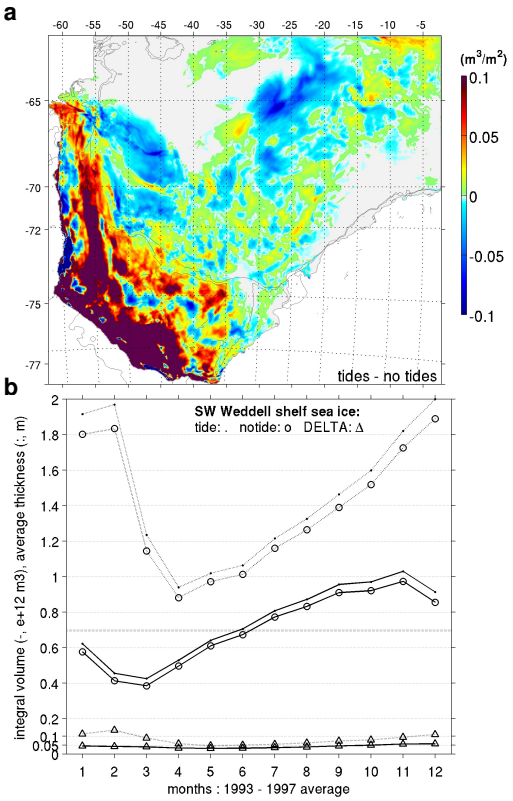


**Figure 10 | Impact of tides on southwestern Weddell sea-ice distribution**, estimated from the year 4-8 5-year average of the reference versus no-tide simulations. **a** Map of the tidal signal $\Delta$ in February sea-ice volume (divided by grid-cell area). **b** 5-yr average monthly timeseries of the southwestern Weddell continental shelf (east of 25°W, south of 62.5°S, and inside the 1500 m isobath) integral sea-ice volume (solid lines, in $10^{12}$ $m^3$ – as reference the horizontal dotted line shows the volume of a 1 m slab covering the whole region) and average sea-ice thickness (actual thickness, not volume per area, dotted lines): with tides (dots), without tides (circles), and the tidal signal $\Delta$ (triangles).